ILMATIETEEN LAITOS
METEOROLOGISKA INSTITUTET
FINNISH METEOROLOGICAL INSTITUTE

EUMETSAT

# EUMETSAT

# Atmospheric Aerosol Optical Depth retrieval performance from Sentinel-3 SLSTR

# SARP

CONTRACT EUM/CO/19/4600002237/JCh

## Report 3

March 25, 2021

Authors: Pekka Kolmonen, Timo Virtanen (FMI)

Version 4.1 (Final)

This deliverable replaces deliverables [D-4] – [D-10] for Option 1.

**DOCUMENT STATUS SHEET**

| | FUNCTION | NAME | DATE | SIGNATURE |
|---|---|---|---|---|
| LEAD AUTHOR | editor | Pekka Kolmonen, FMI | 25th March 2021 (version 4.1) | |
| CONTRIBUTING AUTHORS | | Larisa Sogacheva, FMI<br>Timo Virtanen, FMI<br>Antti Lipponen, FMI | | |
| REVIEWED BY | PI | Timo Virtanen, FMI | | |
| APPROVED BY | Technical officer | Julien Chimot | | |

**VERSION HISTORY**

| Version | Contents | DATE |
|---|---|---|
| 1.0 | The original version | 26th August 2020 |
| 2.0 | Expanded the description of the 555/1610 nm k-ratio method. Minor typo corrections. | 9$^{th}$ September 2020, Pekka Kolmonen |
| 3.0 | A major restructuration of the report. Addition of the results and/or discussion of the action items of the option project. | 13$^{th}$ December 2020 |
| 4.0 | Revision based on feedback | 12$^{th}$ February 2021 |
| 4.1 | Final revision | 25$^{th}$ March 2021 |

# Summary

The purpose of this document is to report the work achieved within the frame of the so-called Option 1 phase of the SARP project (contract EUM/CO/19/4600002237/JCh), present results, draw conclusions and provide recommendations to the enhancement of the SLSTR aerosol optical depth retrieval performance.

All the work and the results are derived from & hence primarily representative of the FMI (Finnish Meteorological Institute) aerosol retrieval algorithm. The retrievals are done with the proprietary SDV/SSV (SLSTR Dual View/SLSTR Single View) algorithm. The SDV algorithm is applied over land while the SSV algorithm is applied over water [D-3].

The work has been concentrated on three specific issues in the SLSTR AOD retrieval:

1. **Spectral k-ratio studies**. The leading idea is to develop an empirical spectral k-ratio model as function of the viewing geometry and other parameters. Initial spectral k-ratio values are sought with simulation studies. The spectral *k*-ratio tests were limited, and a new spectral *k*-ratio method utilizing ratio of the measured *k*-ratios at 1610 and 555 nm was developed and tested at a proof-of-concept level.
2. **L1B calibration/L2 requirements**. Sensitivity of aerosol retrieval to calibration errors is studied with simulations and actual L1B retrievals using the updated SLSTR calibration data. From the simulations, it was concluded that no more than 0.5% – 2.75% (depending on channel) of relative error can be tolerated for the over land SDV algorithm. For the over ocean algorithm, the error in the retrieved AOD is directly proportional to the calibration error as the algorithm uses only single view together with a modeled spectral ocean surface model. In the actual L1B retrievals, the new calibration correction proved to enhance the AOD retrieval in visual evaluation as well as in validation.
3. **The effect of wind speed on AOD retrieval over ocean.** The SSV retrieval is improved by replacing the wind speed climatology with the ECMWF wind speed forecast data. The use of new parameterization of whitecap fraction is studied. The effect of these changes to the AOD over ocean is presented.

# Contents

## List of figures

## Applicable documents

[AD-1] Statement of Work for Atmospheric Aerosol Optical Depth retrieval performance from Sentinel-3 SLSTR, Doc.No.: EUM/RSP/SOW/18/984723, Issue: v1, Date: 29 March 2018.

[AD-2] Generic Statement of Work for Level 2 Product Evolution/Development Studies, Doc.No.: EUM/TSS/SOW/18/1018464, Issue: v1A, Date: 4 September 2018.

[D-2] Atmospheric Aerosol Optical Depth retrieval performance from Sentinel-3 SLSTR, SARP, Report 1, Version 2, EUMETSAT, 2020.

[D-3] Atmospheric Aerosol Optical Depth retrieval performance from Sentinel-3 SLSTR, SARP, Report 2, Version 2, EUMETSAT, 2020.

# Investigation of the SLSTR dual-view geometry in aerosol retrieval

This section describes the actions extended during the Option 1 of the SARP study in view of further understanding the contribution of the dual-view characteristics of the SLSTR instrument to the performance of the AOD retrieval. These actions potentially help to provide solutions to enhance the performance in unfavourable retrieval geometries in which the resulting AOD has not yet reached acceptable accuracy. For the performance studies, this document is a continuation of the previously delivered documents [D-1] and [D-2]. For better readability, large parts of the related actions and results can be found in the appendix “Simulation studies related to the geometrical issues of the retrieval”. In that section additional information about the applied SLSTR Dual View (SDV) algorithm and the treatment of e.g. Rayleigh scattering correction is given.

## Additional extended simulations

In the main part of the SARP project, simulations were originally limited to no variation in the viewing zenith angle of the nadir view. This omission could lead to conclusion that the AOD retrieval performance is dependent only on the oblique view geometry and especially on the oblique relative azimuth angle. To amend this part, full angle simulations were computed with the same radiative transfer algorithm as in the previous & main phase of SARP (see [D-2]).

The new simulation data set was computed for all land surface covers and four months described in [D-2], and the resulting data set was delivered to EUMETSAT. In agreement with EUMETSAT & with respect to the allocated Option 1 resources, the extended geometry data set was restricted to the weakly absorbing fine particle model. The rationale of this choice is the relative abundancy of such particles in ambient continental conditions. Additional data sets can in principle be produced for other types of aerosols.

The nadir viewing zenith angle was varied in the range from 0 to 30 degrees. This range covers most of the cases occurring in the actual SLSTR L1B data. The oblique viewing zenith angle was kept at 55° as the variance of this angle is negligible in practice. It should be emphasized that the resulting viewing geometry data set is not the same for the nadir and oblique views. Although the range of scattering angles obtained for each view is similar, they are obtained using different sets of relative azimuth angles and hence the surface reflectance contributions differ. Therefore, we do not expect the resulting AOD error plots to be symmetric with respect to the x- (oblique view scattering angle) and y-axis (nadir view scattering angle).

The relative AOD error in the retrieval using the extended geometry simulations is shown in Figure 1 for the cropland surface type in July. The results for other surface types and months are shown in the Appendix “The retrieval results of the full angle simulations”. For a comparison, Figure 2 shows the same sort of error distribution as in Figure 1 for the actually retrieved AOD with the SDV (S3A SLSTR L1b data) and ADV (AATSR L1B). For the SLSTR the results are aggregated from July-August 2018 and for AATSR from August 2010. Similarities to the results can be observed, although more AOD should be aggregated for a quantitative comparison.

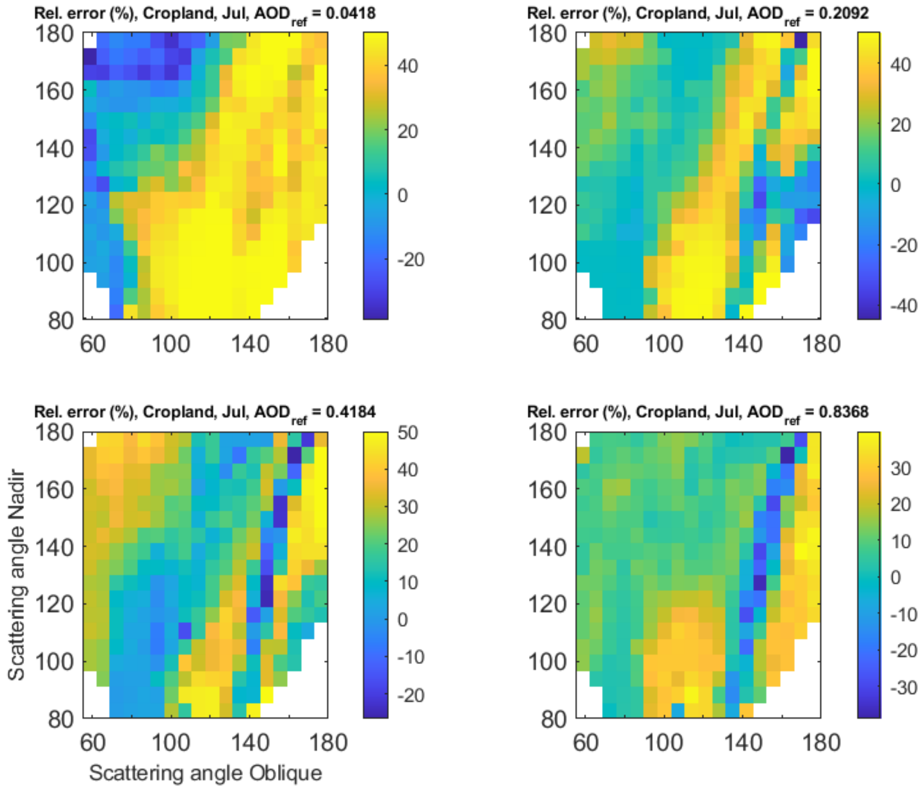


*Figure 1 The relative error in the retrieval of the simulated TOA reflectance for four reference AOD values. Surface is cropland (July) and the aerosol model consists of the weakly absorbing fine particles.*

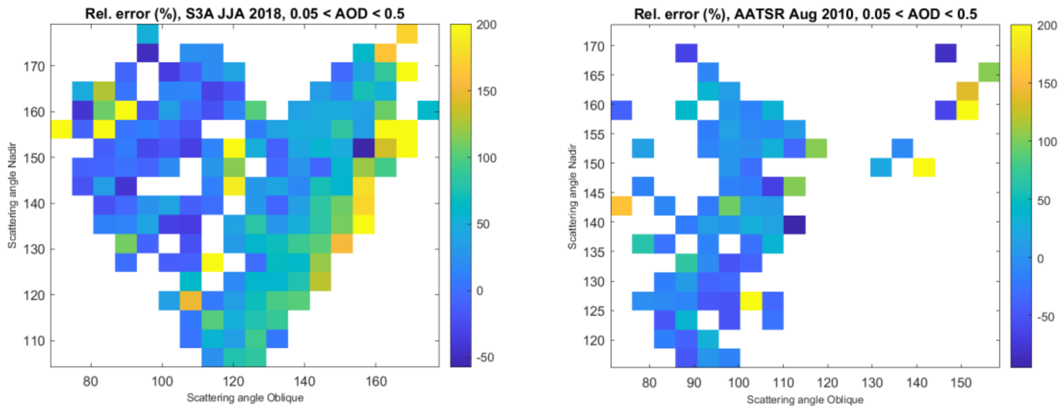


*Figure 2 The relative error in the retrieval with the SLSTR and AATSR data. Left -- S3A SLSTR SDV. Right -- AATSR ADV.*

In previous analysis of the project, the poor performance of the AOD retrieval was primarily connected to the relative azimuth angle in the oblique view. As can be observed in Figure 1, the constrained geometry, while being very informative, does not give all the information. In the nadir/oblique scattering angle space overestimation of the AOD can be seen at large values of the nadir scattering angle while the values of the oblique scattering angle are small. A narrow vertically oriented area of underestimation can be seen for the three of the reference AOD values ($AOD_{ref}$ = 0.0418 excluded). This phenomenon has been recognized in previous work and can be seen also in Figure 3, and is specifically related to the unfavorable geometry (i.e. high scattering angle) of the oblique view only.

## The utilization of the 2250 nm channel within the SDV algorithm

A short study was conducted to find out if there is additional value of including the 2250 nm channel into the over land SDV algorithm. The use of this channel for the *k*-ratio computation was similar to that of the use of the 1610 nm channel except that the TOA reflectance signal is generally significantly smaller, and thus more prone to measurement errors in the L1B data, at 2250 nm. No additional benefit was found for the SDV algorithm and further development was stopped. For a different type of retrieval relying more on absolute spectral constraints per single view (MODIS dark target approach), this channel can be used to derive information on the surface reflectance at shorter wavelengths.

## Spectral *k*-ratio approach

The original objective of this option project was to improve the *k*-ratio method by additional constrains or alternative formulation to enhance the AOD retrieval in the conditions where the basic SDV algorithm performs erratically. The obvious course of development to achieve this was to use the actual surface reflectance from the simulations to set the *k*-ratio for each wavelength utilized in the retrieval. In effect, this approach discards the process in the SDV algorithm of determining the *k*-ratio at 1610 nm and then assuming this ratio to be constant for the whole utilized spectrum. If this approach was to result in reliable AOD some general spectral and perhaps surface dependent constraint would then be derived for the actual aerosol retrieval using SLSTR L1B data. This idea, however, did not prove to be successful in the simulated retrievals; there was no detected enhancement in the accuracy of the resulting AOD as can be seen in Figure 3.

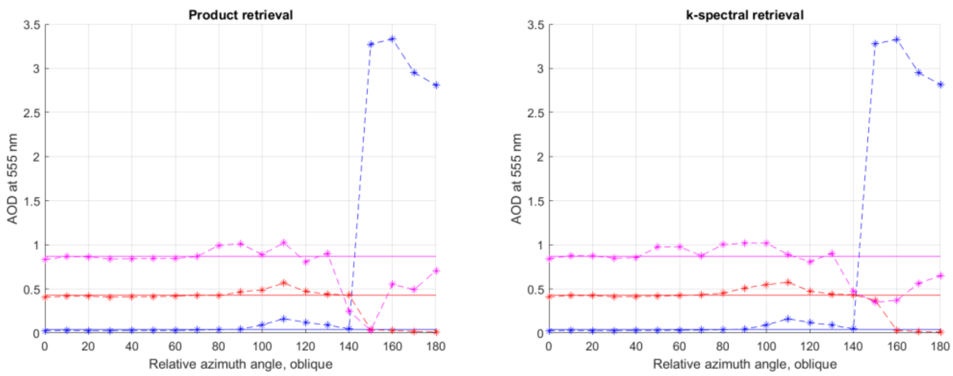


*Figure 3 The comparison of the basic SDV algorithm (Product retrieval) and the spectrally set k-ratio retrieval (*k-spectral retrieval*). Three different reference AODs are shown as a function of the relative azimuth angle in the oblique view: blue (0.04), red (0.42), and magenta (0.84). The sun zenith angle is 45°, viewing zenith angle in nadir view is 0° and in oblique view 55°. Surface is cropland in July and the aerosol model is the urban/background model.*

The basic reason for the poor performance has been understood within the SARP project to be related to the weak aerosol signal in certain geometries (see [D-2]). The inclusion of the exact spectral *k*-ratios did not lead to better performance.  This is now understood to be related to an implicit assumption in the SDV algorithm. Simplifications are made on how the different surface reflectance components and transmittance to TOA level are treated in SDV, as detailed in the Appendix. These simplifications are necessary to allow the use of the k-ratio approach, but they lead to intrinsic errors in the retrieval. While these errors are small, they affect the retrieval performance in the back-scatter geometry region where the aerosol signal is weak.

In practice, the surface reflectance term used in SDV does not correspond to the direct surface reflectance component (BRDF term), but includes components of diffuse surface reflectance, and remains somewhat ambiguous. This ambiguity means that applying the spectral k-ratios obtained from the simulated (direct) surface reflectance data do not fit perfectly the SDV formalism. Hence, the use of spectral k-ratio does not completely remove the intrinsic errors, and the SDV performance is not improved.

Figure 4 illustrates the intrinsic errors in terms of the SDV cost function. The cost function is used in the inversion to find the aerosol model that best fits the measurements, by minimizing the difference in TOA reflectance between the observations (simulations in this case) and the SDV forward model (square sum over wavelengths). The black lines show the cost function for the true aerosol model (i.e. the one used in creating the simulated TOA reflectance). Ideally, this should be zero, but due to the assumptions made in SDV it has a finite non-null value. The colored lines show the cost function for wrong aerosol models, for AOD=0.25 (blue) and AOD=1.0 (red), when the true value is 0.50 (black). We see that for RAZ>120° the cost function for wrong aerosol model is lower than for the true one, causing erroneous retrieval results. The solid lines show the cost function for the spectral k-ratio approach, while the dotted lines show the results for the product approach. We see that the absolute magnitudes are different between the approaches, but the relative values between the correct and wrong aerosol models behave similarly, such that the retrieval fails at large RAZ. Note that this is a simplified example where the aerosol model has been frozen: in reality the aerosol model is retrieved simultaneously with the AOD level, which would make the cost function comparison much more complicated.

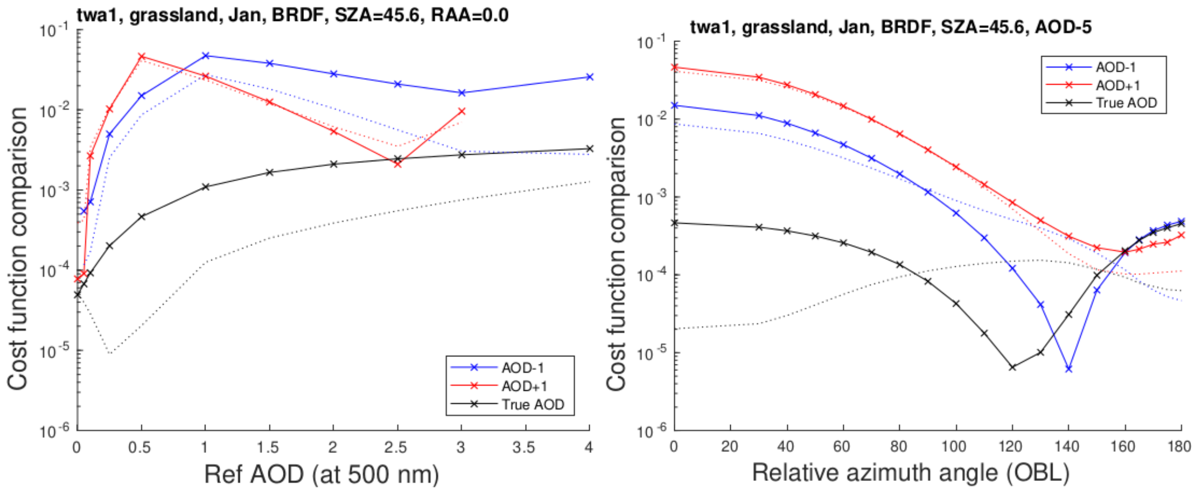


*Figure 4 SDV cost function comparison between product version and spectral-k approach.*

The “blind spot” for aerosol retrieval can be seen as equal cost function values for different aerosol loads at large relative azimuth angles. On the other hand, we see that the cost function can be slightly ‘tuned’ by changing the retrieval approach, *e.g.* by using spectral constraints. However, it is difficult to find an approach which would lead to general improvement for the varying geometries, aerosol conditions, and surface types. Instead, an approach targeted specifically for the back-scatter region was developed. This method is described in the next sub-sections.

### Utilizing measured spectral TOA signal together with *k*-ratio approach to enhance the retrieval performance

Here the possibility of using spectral *k*-ratio computed from the **measured** TOA reflectance is studied. Note that the *k*-ratio determined here is not anymore defined as the oblique-nadir ratio of the surface reflectance but there is also the contribution of the atmosphere which includes the aerosol contribution, especially at visible part of the spectra, which is the object of interest. This *k*-ratio is here denoted $k_{tot}(\lambda)$ as it is computed using the total TOA signal. Note that because $k_{tot}(\lambda)$ is now wavelength dependent, there is λ in the denotation. Note also that if the aerosol model under study is comprised of fine particles $k_{tot}$(1610 nm) can still be understood to be the surface only *k*-ratio because the contribution of aerosols to the TOA signal is small at NIR.

In practice, a LUT which maps the spectral *k*-ratio ($k_{tot}(\lambda)$) to the AOD is determined from the simulations and this LUT can then be applied in the AOD retrieval. Next the method is described, and limitations are discussed. Finally, an example of the LUT and retrieval method are presented.

Figure 5 shows the TOA reflectance with AOD(550 nm) = 0.42 over a cropland surface. The reflectance is plotted for two aerosol models, the urban/background and smoke, to show the variance in the TOA reflectance even though the aerosol loading is equal between the models. The variance comes from the difference in the optical properties of the particles; the aerosol particle size distributions are identical.

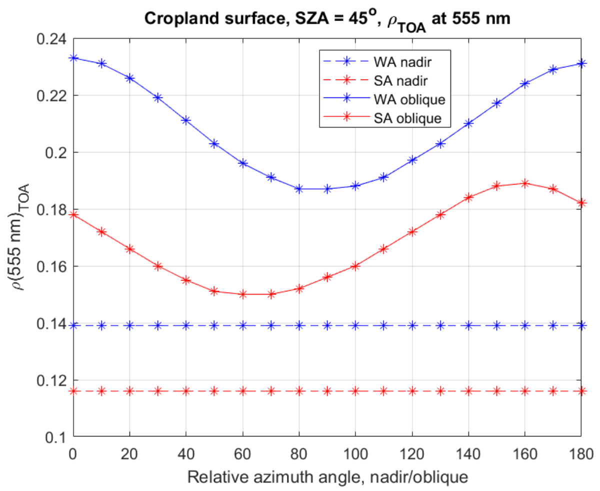


*Figure 5 Example of the simulated TOA reflectance at 555 nm for the nadir and oblique views, and for two aerosol models: WA is the **urban/background** model and SA is the **smoke** model. The surface type is cropland, sun zenith angle is 45 degrees, viewing zenith angle in nadir view is 0° and in oblique view 55°, and AOD at 555 nm is 0.42.*

In Figure 5 it can be observed that the optical properties of the aerosol models affect the TOA reflectance. For strictly nadir viewing angle (*i.e.* 0 deg), the dashed lines, the reflectance is independent of the relative azimuth angle – a constant difference between the reflectance of the two views can be seen. For the oblique view, the solid lines, the TOA reflectance shows a curve where the contribution of the aerosol phase function and surface BRDF both contribute. Here only one surface type is shown. For another surface the constant reflectance value in the nadir view and the amplitude and shape of the oblique TOA reflectance would most probably be different from those seen in the figure. Thus, the two largest challenges, excluding cloud screening, of the retrieval of the optical properties of the atmospheric aerosol are

- How to treat the unknown surface?
- How to know which aerosol model is correct?

The *k*-ratio method used in the SDV algorithm attempts to solve the first challenge. The aerosol model in SDV is handled by a mixture of a priori aerosol model information (average monthly dust fraction), and with the spectral dependency of the TOA reflectance on the aerosol model size distribution and refractive index. For the latter aspect, Figure 5 seems to indicate that there is some geometry related difference between the TOA reflectance of the two aerosol models. This information is not, however, possible to utilize in a real data retrieval as there is only one value sampled from the angle domain for a given surface pixel and date/time.

The method described here is based on the hypothesis that

- ***The variation in the spectral k-ratio between different aerosol models is small enough to allow the use of an average ratio as a proxy for the AOD***.

Figure 6 shows that at certain geometries, here when the oblique view relative azimuth angle has values above 100 degrees, the variation in the *k*-ratio is quite small (which is also part of the problem why the SDV algorithm has a poor performance in these geometries). In addition, land ***surface reflectance is considered by using the 1610 nm k-ratio, where aerosol contribution is minimal, as a normalization factor***.

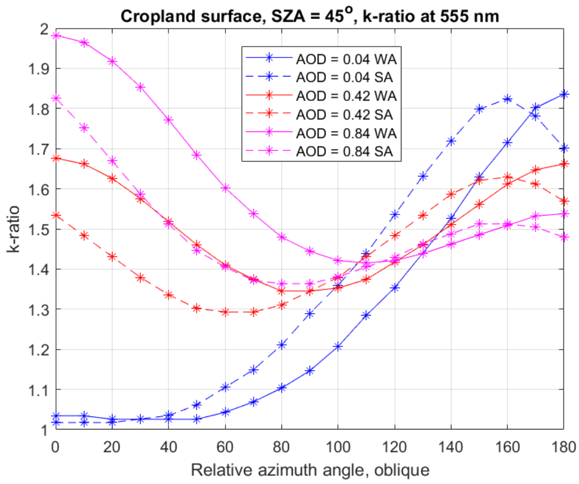


*Figure 6 Variation of the k-ratio as a function of the AOD at 555 nm for two different aerosol models: WA is the **urban/background** model and SA is the **smoke** model.*

The method is a hybrid spectral – dual geometry constraint utilization as described in Figure 7, and can be briefly summarized as:

- Assume that any aerosol model can be considered as a reasonable average representative of the ensemble of possible aerosol models.
- Assume that the land surface pixel has an approximately known cover type.
- The AOD at 550 nm can be determined by comparing the $k_{tot}(\lambda)$ at 550 nm and 1610 nm. Here *surface contribution comes from the 1610 nm ratio* and the *surface + atmosphere contribution comes from the 550 nm ratio*.

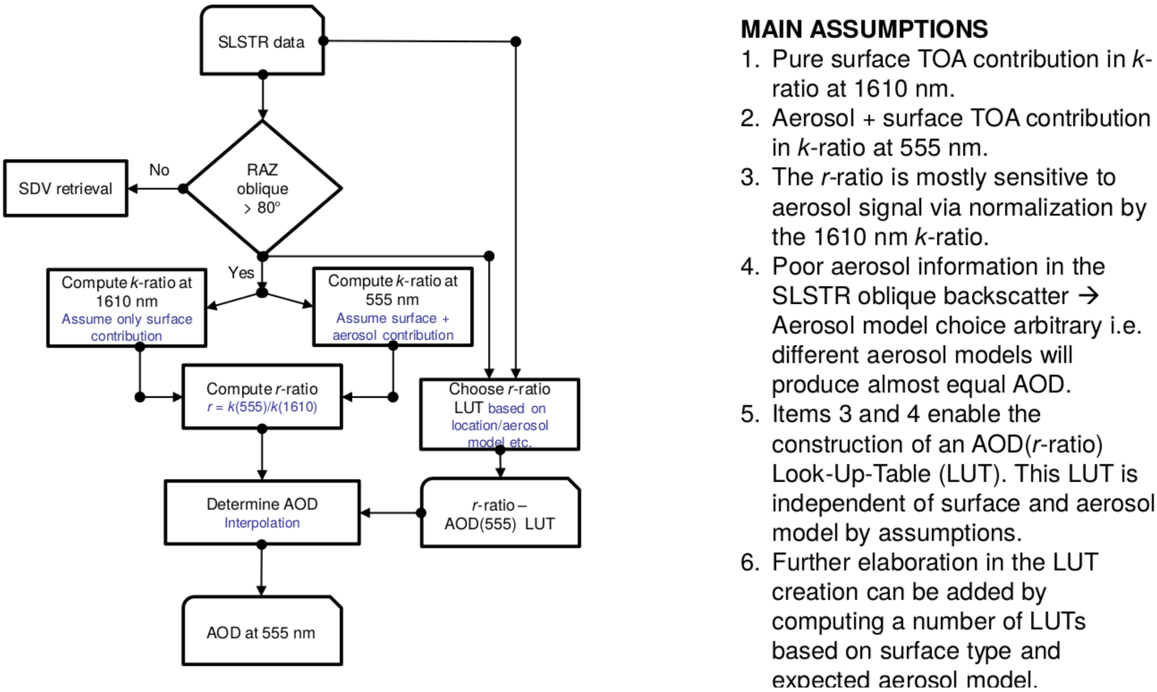


*Figure 7 Description of the r-ratio method.*

The above mentioned comparison can be defined, for instance, with a ratio

$$r = \frac{k_{tot}(550\ nm)}{k_{tot}(1610\ nm)}.$$

Another possibility to carry out the comparison could be to compute difference or relative difference of $k_{tot}$.

As an example, Figure 8 shows what the ratio *r* looks like in the geometrical situations that have been previously studied in this work. The example is determined for the cropland surface with three different aerosol models (urban/background, smoke, dust) to study how uniform the ratio is between extremely varied aerosol conditions. Several observations can be made when studying the figure:

- The geometry of interest in this study starts at around 80 degrees in the oblique view azimuth angle (corresponding approximately to a scattering angle of 120° for 45° SZA). There is interesting information below this value, but it will be excluded here.
- For the urban/background and smoke aerosol models the *r*-ratio has roughly similar features.
- When the AOD value is increased the *r*-ratio for dust starts to deviate from the ratios of the two other aerosol models. This is inevitable as the aerosol signal starts to affect the TOA signal at 1610 nm where we still assume that the instrument sees pure surface.
- There is a certain retrieval geometry at around 120 to 140 degrees of oblique azimuth angle where the r-ratios at the highest and lowest AOD values are almost identical for the urban/background and smoke aerosol models. This is the "blind spot" where the atmospheric signal vanishes and the AOD retrieval may be impossible with this sort of a method. This can be seen also in Figure 43 where the retrieved AOD loses most of the sensitivity in oblique azimuth angles of 120 - 140 degrees.

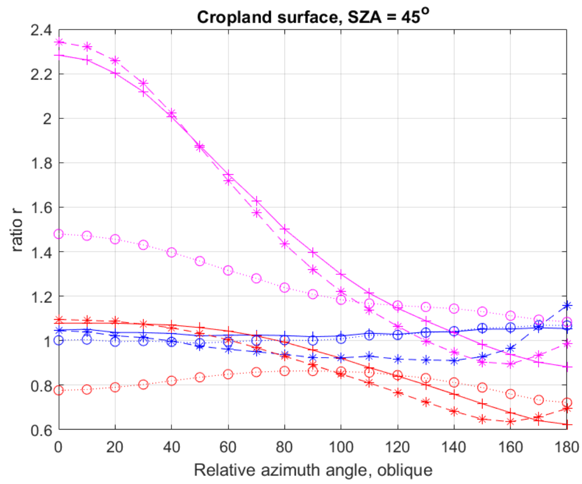


*Figure 8 An example of the sensitivity of the r-ratio with atmospheric contribution to the AOD. The ratio r is plotted as a function of AOD (three values) and the azimuth angle of the oblique view. The AOD at 550 nm are 0.04 (blue), 0.42 (red), and 0.84 (magenta). There are three different aerosol models: urban/background (+), smoke (*), and dust (o).*

Next step is to test the described method in the retrieval of the AOD in the challenging geometries. Furthermore, this method uses only satellite measured TOA signals. A priori knowledge about the spectral surface *k*-ratios could be combined with this approach. As an example, a test retrieval was done where the *r*-ratio was utilized. In this example the same surface class and aerosol model was used in creating an AOD LUT for different *r*-ratios and in the retrieval. The chosen surface class was cropland and the aerosol model was the urban/background one. A cross-testing can then be arranged by mixing different surface classes and aerosol models in the computation of the *r*-ratio and retrieval.

In addition, a test was constructed where, for the cropland surface with a simulated TOA reflectance having the contribution of the urban/background aerosols, the *r*-ratio was determined by a 50/50 mixture of the simulated *k*-ratios of the urban/background and smoke aerosol models. The *r*-ratios for the two models as functions of the AOD are presented in table 1 and plotted in Figure 9 for a geometry where sun zenith angle is 45°. The relative azimuth angle in the oblique view is here 140° - 180° and the *r*-ratio is the average of the ratios in the angle range.  This table is used as a LUT connecting the AOD and the *r*-ratio. In practice, the LUT is dependent also on the retrieval geometry and a possible weaker surface type dependence may have to be included. Note that also the AODs differ between the aerosol models which leads to using the 50/50 mixture for the AOD. To add more uncertainty a 10% relative error was added to all TOA reflectance employed in the determination of the *r*-ratios.

Figure 10 shows the results of the ***r*-ratio retrieval**. For comparison, see the results of the **product retrieval** and ***k*-spectral retrieval** in Figure 3.

*Table 1. The r-ratios and AODs at 550 nm for the urban/background and smoke aerosol models. Sun zenith angle is 45°, surface is cropland, and month is July.*

| Urban/background AOD | Urban/background *r*-ratio | Smoke AOD | Smoke *r*-ratio |
|---|---|---|---|
| 0.0418 | 0.8858 | 0.0433 | 0.8845 |
| 0.0837 | 0.8908 | 0.0867 | 0.8883 |
| 0.2092 | 0.9095 | 0.2167 | 0.9025 |
| 0.4184 | 0.9425 | 0.4333 | 0.9286 |
| 0.8368 | 1.0000 | 0.8666 | 0.9708 |
| 1.2553 | 1.0459 | 1.2999 | 1.0016 |
| 1.6737 | 1.0833 | 1.7333 | 1.0247 |
| 2.0921 | 1.1144 | 2.1666 | 1.0418 |

| | | | |
|---|---|---|---|
| 2.5105 | 1.1396 | 2.5999 | 1.0548 |
| 3.3473 | 1.1763 | 3.4665 | 1.0709 |

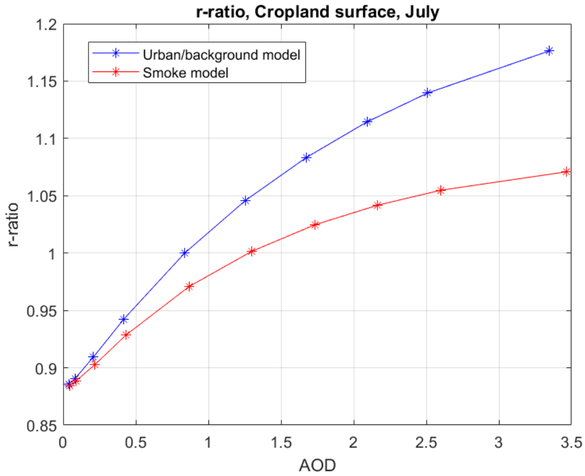


*Figure 9 The r-ratio as a function of the AOD from table 1.*

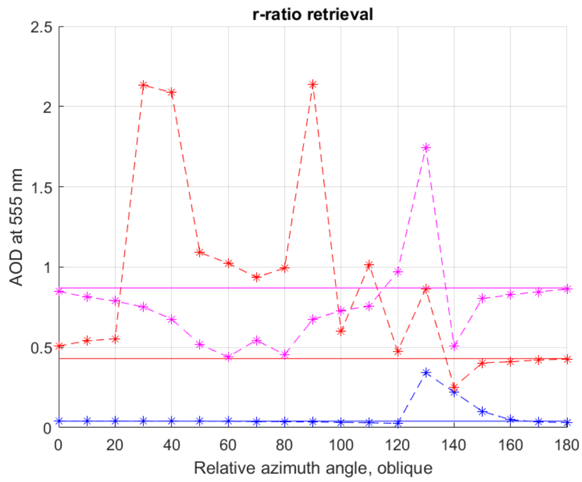


*Figure 10 The **r-ratio retrieval**: AOD at 555 nm with the Urban/Background aerosol type over the BRDF cropland surface as a function of the relative azimuth angle of the oblique view. Horizontal lines indicate the reference AOD values of 0.042 (blue), 042 (red), and 0.84 (magenta). Sun zenith angle is 45°.*

The *r*-ratio seems to manage a quite good retrieval in a geometry where the variation of the ratio is small (large values of the oblique relative azimuth angle) which is to be expected when the method is studied (see Figure 8). The benefit of the *r*-ratio is that it potentially provides well-behaving retrieval in the situations where the baseline *k*-ratio algorithm has problems. In contrast, in the angle range (oblique relative azimuth less than 130°) where there is more information available, the *r*-ratio retrieval fails because the assumption of small difference between the aerosol models is not valid; the correct identification of the aerosol model is crucial for accurate AOD retrieval. Note: in this retrieval example two separate *r*-ratio LUTs were used

1. LUT for the oblique relative angle range of 140° - 180° which is shown in table 1 and Figure 9.
2. LUT for the oblique relative angle below 140° which is not shown here.

The development of this alternative method to determine AOD in the challenging geometries was decided to be kept at the proof-of-concept level described here.

### Discussion of the geometry effects studies

This work aims to study the effect of the retrieval geometry on the resulting AOD from the SDV algorithm, and, more importantly, to find methods to overcome the challenges caused by the dual-view nature of the algorithm in some geometries. Besides surface/atmosphere analysis and the SDV retrieval algorithm descriptions, two methods were described and tested:

- The *k*-spectral method, where the *k*-ratio is computed from known surface reflectance for all employed wavelength. This approach, in principle, should lead to good performance based on the description of the *k*-ratio. This was not the case, however, the results were quite like the baseline product retrieval, where *k*-ratio is determined using the measured 1610 nm reflectance. It was discovered that the use of a spectrally flat k-ratio in the retrieval is not the only cause of poor SDV performance in the challenging geometries. It was further understood that using the spectral k-ratios from the simulated surface data is not an ideal way to apply spectral constraints on the retrieval, and more research on the subject is required.
- The *r*-ratio method, where spectral behavior of the *k*-ratios is used as an indicator of the AOD. The method works quite reliably in geometrical situations where the variation of the *r*-ratio is small enough between aerosol models having differing optical properties (due to chemical composition or size distribution). These geometrical situations are almost exactly those where the baseline and *k*-spectral methods fail.

## The calibration correction of the TOA reflectance at the SLSTR visible and NIR bands

The calibration correction exercise is here two-fold: adding calibration error to simulated TOA reflectance and applying the calibration corrections to the SLSTR L1B reflectance. The calibration corrections in this study refer to the old and the new set of spectral values, and to the way the correction has been applied to the FMI SDV/SSV aerosol retrieval algorithm. Table 2 shows the corrections as applied to SDV/SSV (Smith, 2020).

*Table 2. The old and the new calibration correction factors $c_\lambda$ at the utilized SLSTR nominal wavelengths (Smith, 2020).*

| | 555 nm (nad/obl) | 659 nm (nad/obl) | 870 nm (nad/obl) | 1610 nm (nad/obl) |
|---|---|---|---|---|
| Old correction | - | - | - | 1.134/1.056 |
| New correction | 0.97/0.94 | 0.98/0.95 | 0.98/0.95 | 1.11/1.04 |

In the old correction approach of SDV it was decided to modify only the 1610 nm channel. The reasoning behind this decision was that the infra-red channel is the most important one for reliable retrieval as the *k*-ratio is computed utilizing this channel. *This, in retrospect, seems to have been the wrong approach because the old and new calibration corrections are rather similar at the 1610 nm*. The quite dramatic changes in the retrieved AOD, as shown below in the SLSTR L1B retrievals, are most probably caused by applying the correction to the other utilized channels.

### Simulated calibration error

Here, the effect of calibration uncertainty in the L1 SLSTR data on the AOD retrieval is assessed using simulated data. The aim of this exercise is to evaluate the maximum tolerable uncertainty in the L1 data from the point of view of the L2 AOD retrieval with SDV. The following method was employed:

1. SDV AOD retrieval is performed with unperturbed (zero uncertainty) simulated TOA reflectance data. These AOD data are used as the reference values when calculating the AOD error below. Note that these data contain the intrinsic errors associated in the SDV retrievals.

2. Perturbation (error) is added to the simulated TOA reflectance. The perturbed TOA reflectance $R'_\lambda$ is of the form
$$R'_\lambda = R_\lambda\left[1 + P\left(c_\lambda^{-1} - 1\right)\right]$$
where $R_\lambda$ is the original reflectance, $c_\lambda$ is the calibration coefficient from Table 2, and P is the fraction describing the amount of applied error. Four cases were studied, with P values of 25%, 50%, 75%, and 100%. The applied perturbation follows the spectral and angular distribution of the current calibration coefficients (Table 2).
3. The AOD retrieval is repeated with the perturbed data. The deviation of the resulting AOD from the reference values of the unperturbed case is interpreted as the AOD error.

Table 3 shows the errors P($1/c_\lambda$-1) applied to each channel and each view in the four cases that were studied (P=25%, 50%, 75% or 100%, respectively). We follow strictly the fixed spectral and angular dependence of the original calibration coefficients as shown in Table 2. In other words, we did not study inter-band variability of the calibration uncertainty. However, in a later subsection we discuss a case where the simulated calibration error was applied separately to the nadir and oblique view to assess the potential necessity of symmetric correction between the views.

*Table 3 Relative errors P(1/c-1) added to the perturbed TOA signal (in %).*

| **P(1/c-1)** (%) | **S1 (555 nm)** | | **S2 (659 nm)** | | **S3 (865 nm)** | | **S5 (1.61 µm)** | |
|---|---|---|---|---|---|---|---|---|
| **P** | **nadir** | **oblique** | **nadir** | **oblique** | **nadir** | **oblique** | **nadir** | **oblique** |
| **25%** | 0.77 | 1.60 | 0.51 | 1.32 | 0.51 | 1.32 | -2.48 | -0.96 |
| **50%** | 1.55 | 3.19 | 1.02 | 2.63 | 1.02 | 2.63 | -4.95 | -1.92 |
| **75%** | 2.32 | 4.79 | 1.53 | 3.95 | 1.53 | 3.95 | -7.43 | -2.88 |
| **100%** | 3.09 | 6.38 | 2.04 | 5.26 | 2.04 | 5.26 | -9.91 | -3.85 |

The form of the perturbation, P($1/c_\lambda$-1), was selected such that for the “100 % error” (P=1), we have $R'_\lambda = R_\lambda/c_\lambda$ and the original reflectance $R_\lambda$ is obtained when the perturbed reflectance $R'_\lambda$ *is* multiplied by the corresponding calibration coefficient $c_\lambda$. In other words, the P=100% case corresponds to a situation where the SLSTR L1 data would be used without applying the current recommended calibration correction factors $c_\lambda$. In a similar manner, the “25% error” (P=0.25) case can be understood as a situation where the calibration coefficients have a 25% relative uncertainty. To clarify, in Table 3 the “25% error” describes the perturbation with respect to the current calibration correction terms ($1/c_\lambda$-1), which translates to 0.5 – 2.5% error with respect to the actual measured L1 TOA reflectance, depending on the band and viewing angle. In case P=25% this means, for example, that $R'_{555} = 1.0077\ R_{555}$ and $R'_{1610} = 0.9752\ R_{1610}$ in the nadir view.

## SDV simulations with calibration error

These results only apply to the dual view algorithm over land. The simulation retrievals were run for all surfaces and months, and for two aerosol models: urban/background (full retrieval geometry) and smoke (limited retrieval geometry). Here the results for the urban/background model are shown; for the smoke models the conclusions do not differ.

Figure 11 shows the example of the calibration error effects in the full geometry with a 100% (P=1) multiplicative error associated with the calibration correction per channel (i.e. 100% uncertainty associated with the calibration correction factor) for the cropland surface in July at four reference

AOD values while Figure 12 shows the same results as histograms. To see more details the same cropland in July example is plotted in Figure 13 for a selected geometry for all applied error levels.

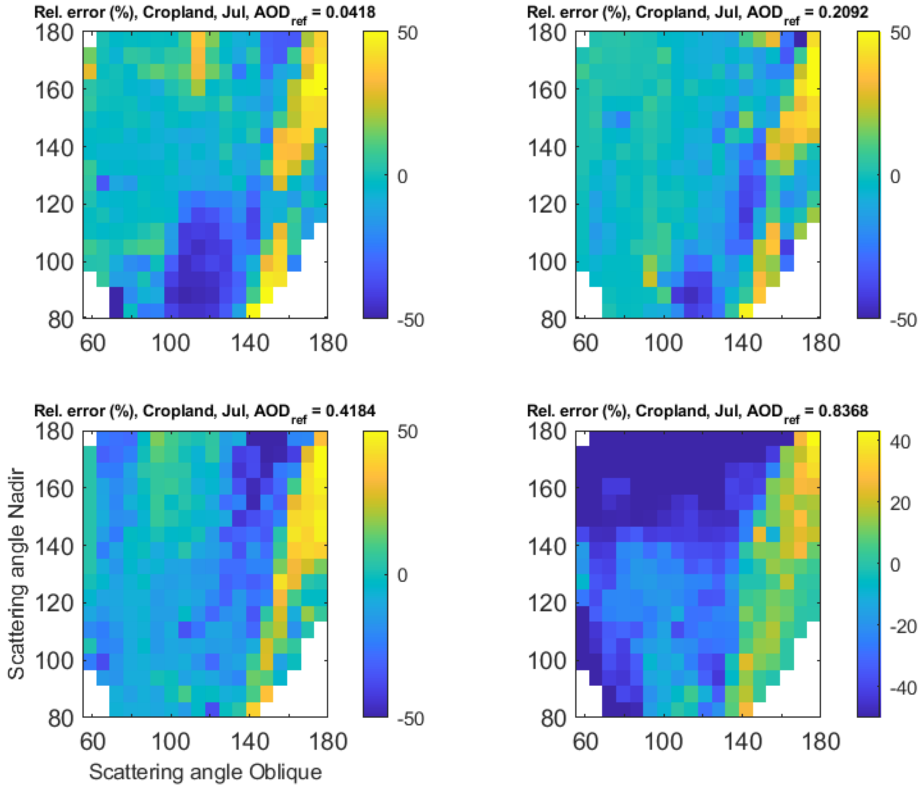


*Figure 11 The relative error as a function of the nadir and oblique scattering angle when 100% of the calibration error is applied. For four reference AOD values, Cropland in July.*

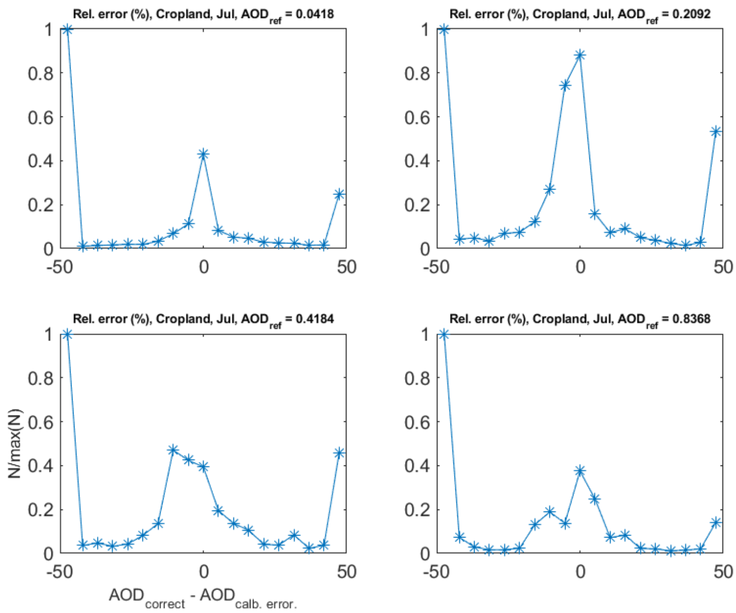


*Figure 12 The histogram of the relative error when 100% of the calibration error is applied. For four reference AOD values, Cropland in July. The error is saturated at ±50%.*

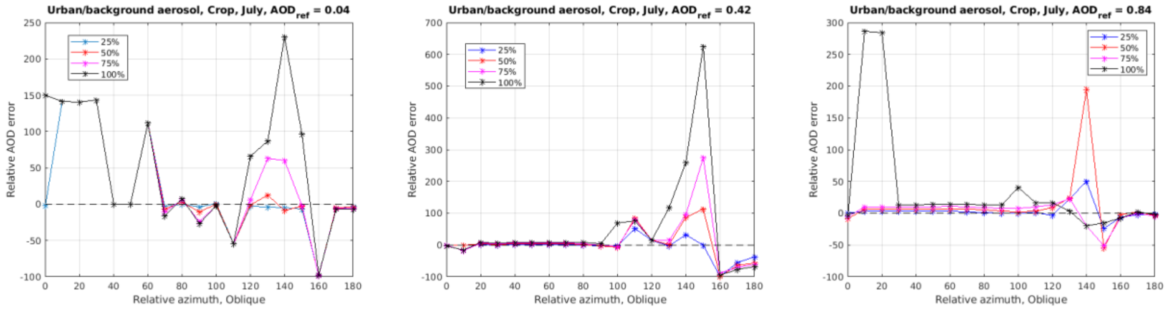


*Figure 13 The calibration error for the cropland in July. Sun zenith angle is 45° and the nadir view zenith angle is 0°. The applied calibration error is 25%, 50%, 75% and 100%.*

The WMO Global Climate Observing System (GCOS) sets the required maximum tolerable measurement uncertainty for AOD at 0.03 or 10% (larger of these) (WMO, 2016). It is not straightforward to propagate this to a requirement on the L1 calibration uncertainty, for the following reasons: 1) The AOD error analyzed here is subject to intrinsic uncertainties in the SDV formalism, and may not represent to true error. 2) The dependence of the AOD error on the applied perturbation to the L1 TOA signal (calibration uncertainty) is complex: increased uncertainty does not always lead to increased AOD error. The dependence on aerosol type, aerosol load, and surface type is complex. 3) The largest AOD error occurs in the aerosol backscatter region (RAZ-Obl > 100°). Tolerance to calibration uncertainty is higher in the less challenging viewing geometries, and aerosol retrieval can fail in the backscatter region even with zero calibration uncertainty.

In the retrievals with simulated data (Figure 11 to Figure 13) we find that in the case of least applied perturbations (25% relative error in the calibration correction coefficients 1/c-1) about 80% of the retrieved AOD values have relative AOD error below 100%. Based on this we conclude that the L1 calibration correction uncertainty should not exceed 25% for any channel. In terms of relative uncertainty of the L1 measured TAO reflectance this corresponds to 0.5 – 2.5% depending on the channel and viewing angle, as detailed in Table 4 below. In this connection it must be emphasized once again that the inter-band sensitivity to the calibration uncertainty was not studied here.

*Table 4. The recommended maximum calibration error tolerated for the SLSTR channels utilized in the SDV/SSV aerosol retrieval.*

| | 555 nm (%) | 659 nm (%) | 870 nm (%) | 1610 nm (%) |
|---|---|---|---|---|
| Nadir view | 0.75 | 0.50 | 0.50 | 2.75 |
| Oblique view | 1.50 | 1.25 | 1.25 | 1.00 |

This conclusion is, however, very much dependent on the retrieval geometry. One the one hand, for a considerable aerosol load (see Figure 13 for AODs of 0.42 and 0.84) there are geometries where the applied calibration error does not cause large error in the resulting AOD; the use of TOA signal from both views makes the SDV algorithm very robust against measurements errors, in principle. On the other hand, if the retrieval geometry has the challenging angles for the SDV algorithm (see Figure 13 for the oblique relative azimuth angle values of more than 100°) even just 25% of calibration error can lead to erratic AOD retrieval. These sorts of geometries generally happen in the Northern Hemisphere for the dual view setting of the SLSTR instrument. Large changes in the retrieved AOD can then be expected in NH if a new set of calibration correction values is applied to the SLSTR L1B data. This will be demonstrated below when the 2020 calibration correction is applied to the actual retrieval using the L1B data.

## Asymmetric calibration error between both nadir & oblique views

To test a situation in which calibration error might be asymmetric, i.e. only one of the views of the dual view instrument is affected by a calibration error, retrievals in a similar geometry as in Figure 13 were run with a 50% and 100% calibration uncertainty. The resulting error in AOD shows differing features between the views (Figure 14). If the calibration error is applied only in the nadir view, the AOD error looks roughly similar as when calibration error is applied to both views, while the inclusion of the calibration error in the oblique view causes an AOD error almost throughout the relative azimuth angle space.

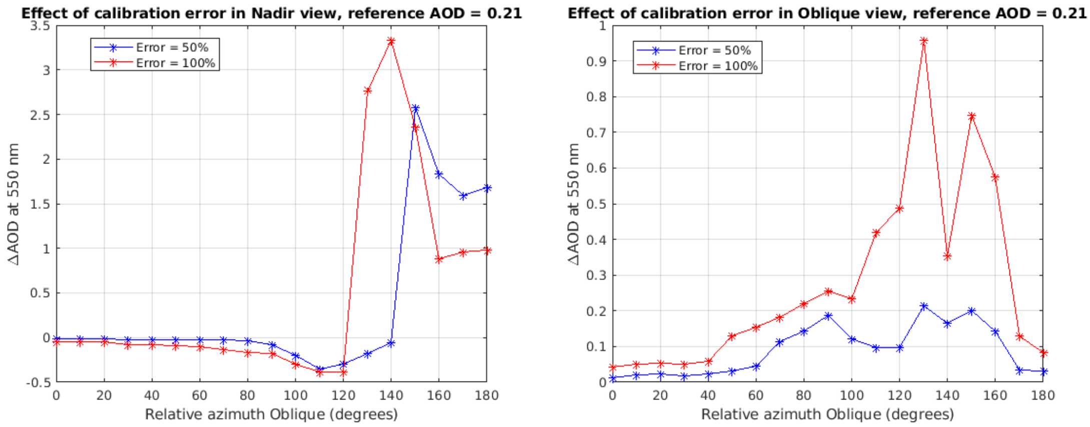


*Figure 14 The asymmetric calibration error for the cropland in July. Left: calibration error applied only on the nadir view. Right: calibration error applied only to the oblique view. Sun zenith angle is 45° and the nadir view zenith angle is 0°. The applied calibration error is 50% and 100%.*

## SSV simulations with calibration error in the special case of dust particles over ocean

It was observed in the main part of the SARP project that the SSV algorithm tends to over-estimate the AOD in heavy dust conditions over water surfaces, such as the transport of Saharan dust across the Atlantic ocean, when compared to the MODIS AOD. Here the addition of calibration error is tested in simulated environment to assess whether the error may cause this over-estimation.

Figure 15 shows a positive bias when the amount of calibration error is increased. If full error (100%) is applied as much as 5% of over-estimation can be detected. This would lead to a positive bias which in part explains the MODIS-comparison results observed previously. In summary, the better the calibration correction is, the smaller the positive bias will be.

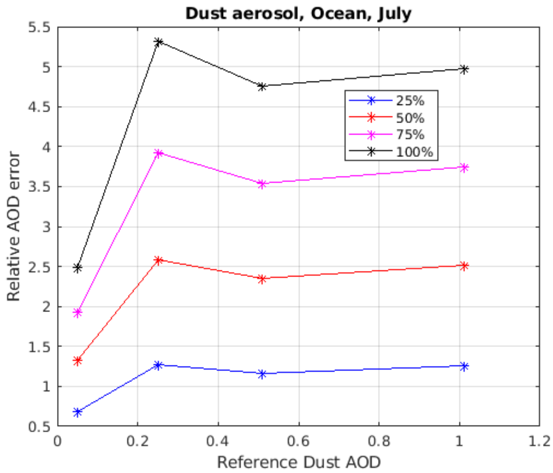


*Figure 15 The calibration error for the ocean surface in July. Sun zenith angle is 45° and the nadir view zenith angle is 0°. Wind speed is 5 m/s. The applied calibration error is 25%, 50%, 75% and 100%.*

## The 2020 calibration corrections applied to aerosol retrieval with SLSTR L1B data

The AOD comparison and validations were started for S3A SLSTR data from year 2018. Unfortunately all planned four months (January, April July, October) were not retrieved with the new calibration correction because of server issues at the local CSC computing center. Results here are divided into detailed analysis for July 2018, and a shorter analysis for April 2018 (see appendix “Summary of the AOD retrieval for April 2018 with the new calibration correction”).

### Average global AOD and a scene comparison, July 2018

The average AOD in July for the old and the new calibration correction is shown in Figure 16, and the difference of the average AODs in Figure 17. Over land the most striking difference can be observed over the land areas in the Northern Hemisphere. With the new correction, the unrealistically high average AOD values are decreased to more modest values. Over oceans, the difference is not as substantial.

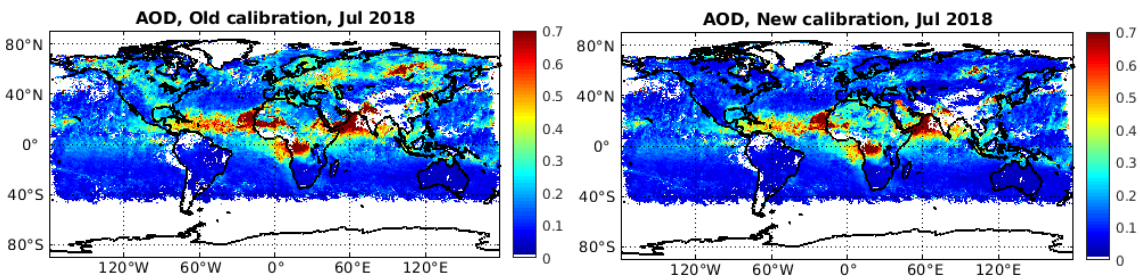


*Figure 16 Average AOD in July 2018 for the old and the new calibration correction.*

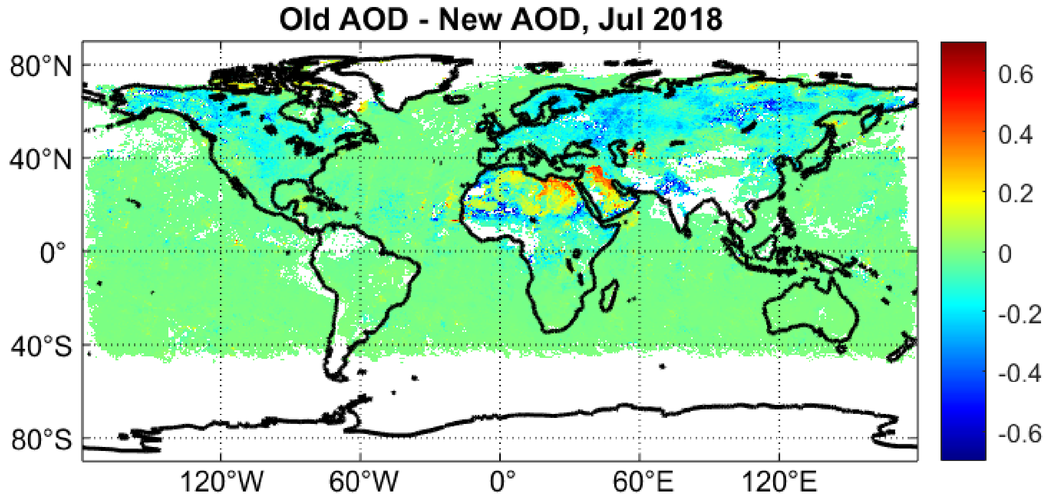


*Figure 17 The difference of the average AOD in July 2018. The AOD applying the new calibration correction is subtracted from the AOD applying the old correction.*

To present the spatial differences between the old calibration and the new calibration at the L2, a SLSTR scene, shown in Figure 18, was chosen. The difference when the old and the new calibration correction can be clearly appreciated in the AOD distribution maps and in the separate over land and over sea comparisons.

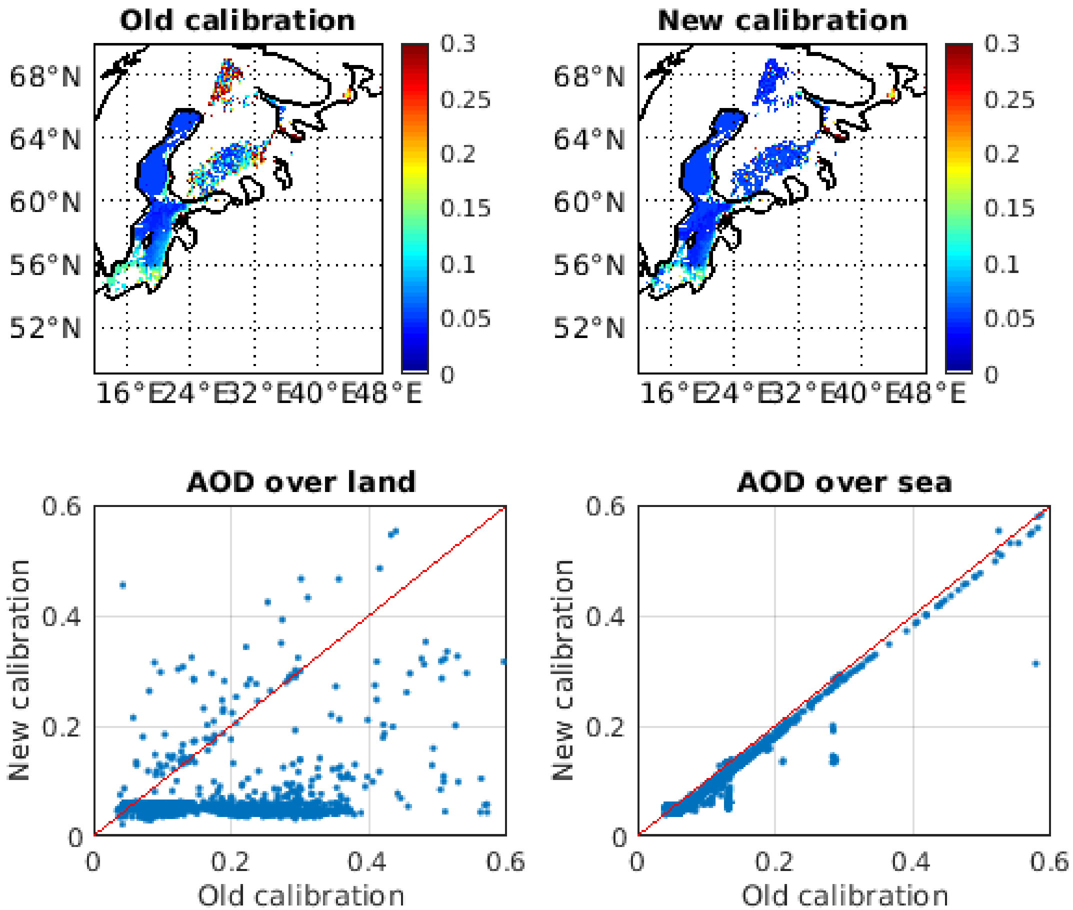


*Figure 18 A L2 comparison of the old and the new calibration correction 1st of July 2019 around 9 o'clock.*

These sorts of comparisons, while educative, are qualitative at the best; comparisons with an independent reference is needed. This is presented next.

## AERONET validation, July 2018

The validation here follows the general procedure: collocate satellite data for a 25 km area around an AERONET site, and ±0.5 hours AERONET data around the satellite overpass. Figure 19 shows the validations of the AOD at 550 nm for the old and new calibration correction. The old calibration shows the features that have already been seen within the SARP project in the SLSTR L1B AOD retrieval validation. The new calibration correction leads to dramatically different validation. There is quite a lot of scatter seen in the comparison but the positive bias from the old calibration correction is gone. Instead, there seems to be a small negative bias for small AOD values.

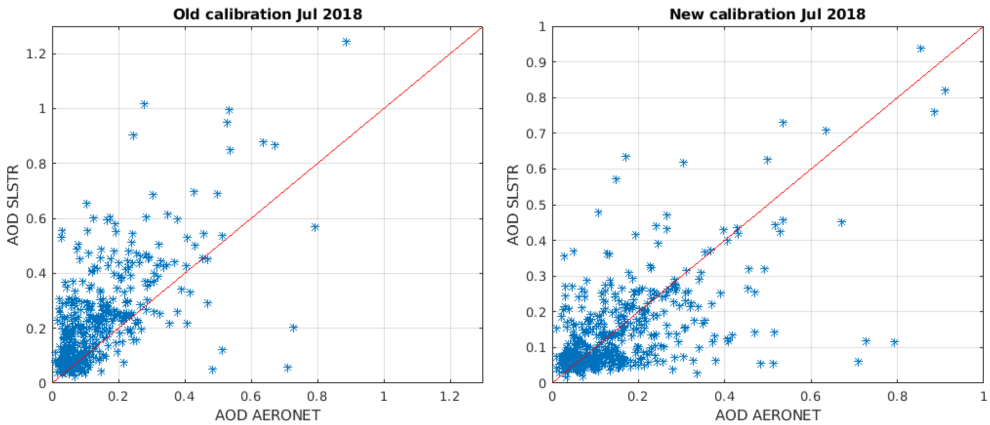


*Figure 19 AERONET validation of the old and the new calibration correction for July 2018.*

To have a more statistical look at the validation, histograms of the validation error for the old and new calibration correction are provided in Figure 20. The slight negative bias can be seen also in the error histogram of the new correction, but the maximum value of the histogram is exactly at zero discrepancy.

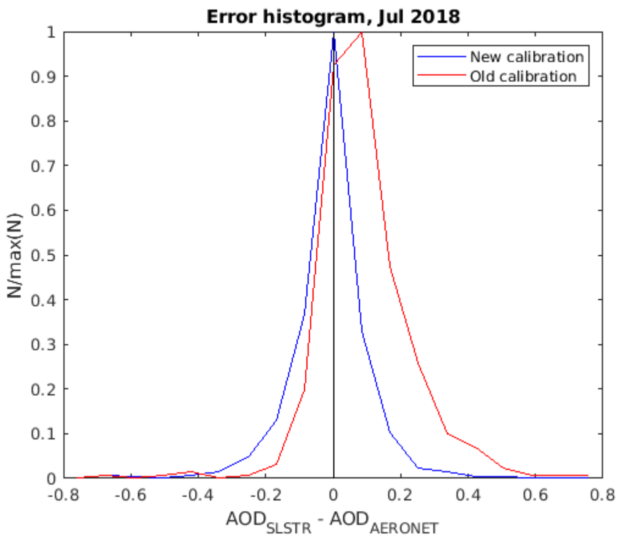


*Figure 20 Histogram of the validation error for the old and new calibration correction, July 2018.*

Still, one more point of view is shown in Figure 21 where the validation error is plotted as a function of the AERONET site latitude. This way the difference between the Southern and Northern Hemisphere can be observed. This difference is connected to the retrieval geometry issue which is one of the subjects under investigation in this project. The North/South division is now less pronounced with the new calibration, but the conclusion is less clear for this type of analysis due to the large difference in the number of AERONET sites between the Hemispheres.

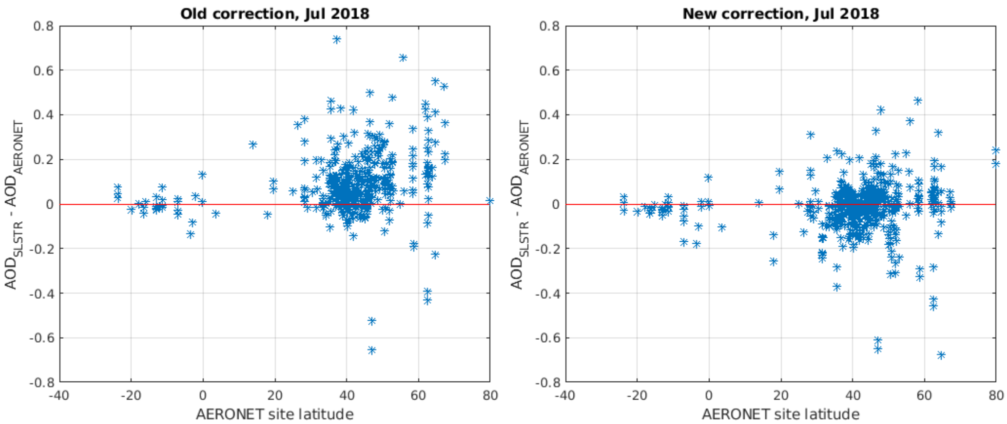


*Figure 21 The validation error for the old and new calibration correction as a function of the AERONET site latitude.*

## Over ocean retrieval

The SLSTR Single View (SSV) aerosol retrieval algorithm uses an ocean surface model which includes contributions from Fresnel reflection, water leaving radiance (chlorophyll) and whitecap reflectance. The SSV algorithm is described in more detail in the Appendix. In SARP Option 1 two improvements were implemented to SSV and tested in retrievals. First, the previously used monthly wind speed climatology was replaced by the ECMWF forecast wind speed data. Second, a new parameterization for the whitecap fraction, depending on wind speed and sea surface temperature (SST), was implemented and tested.

The study is partly motivated by the observed difference between MODIS and SLSTR aerosol retrieval results in rough ocean conditions. The effect of wind speed and the different whitecap fraction parameterizations on SSV retrievals were tested with real S3A SLSTR data for January 2018 for a test region in Southern Atlantic/Southern Ocean (Lon: -60° … 60°, Lat: -60° … -30°). This test case was selected to obtain comprehensive range of wind speed values. Near-simultaneous AOD data from MODIS Terra were used for comparison. Figure 22 shows the mean AOD and wind speed for test area from MODIS and SLSTR.

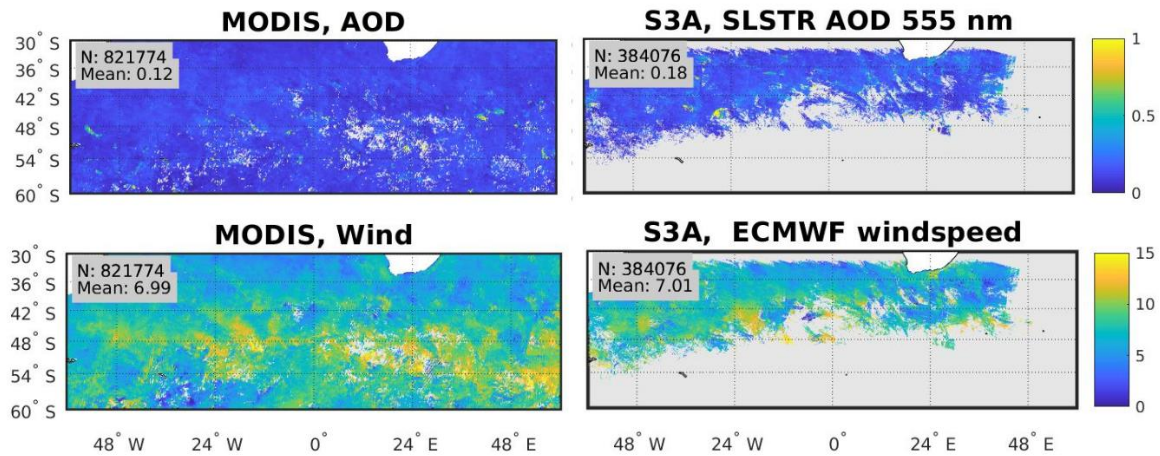


*Figure 22. Monthly mean AOD and wind speed for SLSTR and MODIS for the case study. Mean AOD for MODIS is 0.12 and for S3A 0.18; the mean wind speed for both instruments is approximately 7 m/s.*

We note that there is considerable difference in the coverage between MODIS and SLSTR. Large areas in the southern part of the study area did not contain any SSV aerosol observations due to cloud screening. The frequency of MODIS observations is also reduced in this region, but gaps in data are smaller. Differences in satellite retrieved AOD in the rough ocean conditions are presumably connected with cloud screening issues. In this test case the MODIS AOD was found to be lower than SSV AOD, while in general MODIS has high AOD bias against other satellite products over ocean. One possible explanation is that here we did not apply a cloud post-processing to the SSV data. The post-processing is always performed in the product version to remove residual clouds, and it usually decreases the mean AOD.

## Wind speed

The product version of SSV uses a monthly wind speed climatology from AEROCOM in estimating the whitecap fraction. This is heritage from the AATSR retrieval algorithm, for which timely meteorological data was not easily available. In the Sentinel-era, SLSTR L1B meteorology file includes ECMWF forecast/reanalysis data for wind speed, which was now employed in the SSV algorithm.

The differences between the wind speed climatology and ECMWF data are shown in Figure 23. The difference between ECMWF forecast (NRT) and reanalysis (NTC) are small, and the MODIS wind speed data is similar (not shown). In the comparisons it was observed that the selection of the wind speed data source does not affect the results drastically on the larger scale. Naturally the different wind speed values cause differences in AOD for individual pixels, but on the monthly average level the differences are small.

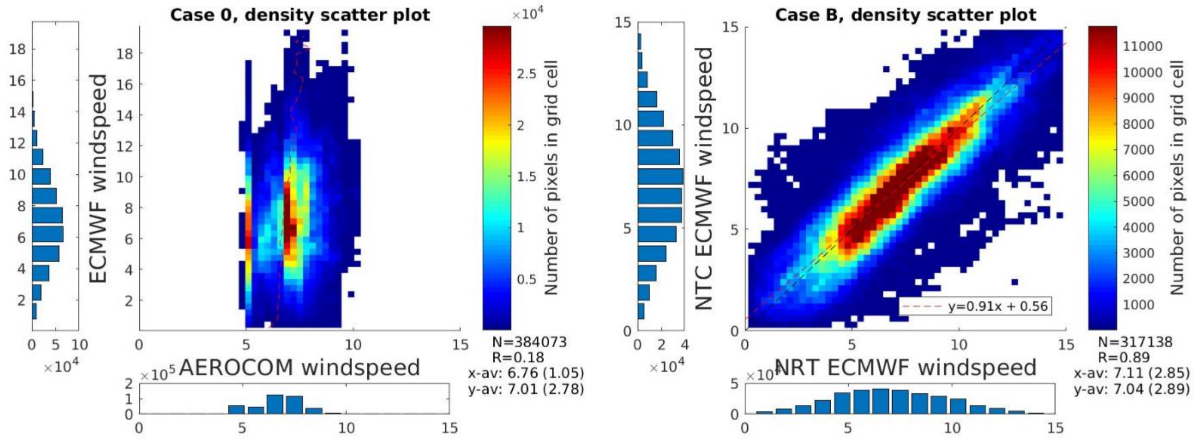


*Figure 23. Difference between the AEROCOM climatology and ECMWF forecast wind speed values, and ECMWF NRT/NTC comparison.*

## Whitecap fraction parametrization

In the SSV surface model the whitecap reflectance is a product of the whitecap albedo and the whitecap fraction W (see the Appendix). In the SSV product version the whitecap fraction *W* is a function of wind speed *u* (Monahan and O'Muircheartaigh, 1980):

$$W = 3.84 \times 10^{-6} \times u^{\,3.41}$$

An alternative parametrization by Albert et al. (2016) was tested in SARP Option 1:

$$W = a(T)\left[U_{10} + b(T)\right]^2, a(T) = a_0 + a_1 T + a_2 T^2, b(T) = b_0 + b_1 T$$

For the parameters $a_0$, $a_1$, $a_2$, $b_0$, and $b_1$ two alternative sets of values are provided, obtained from satellite radar observations at different wavelengths; these are labeled $W_{10}$ and $W_{37}$. This whitecap fraction depends on the sea surface temperature (SST) in addition to the wind speed.

Figure 24 shows whitecap fraction as a function of wind speed for the different parameterizations at three SST values. We see that for larger wind speed values Monahan & O'Muircheartaigh give much larger fraction. We also see that the dependence on SST is rather weak.

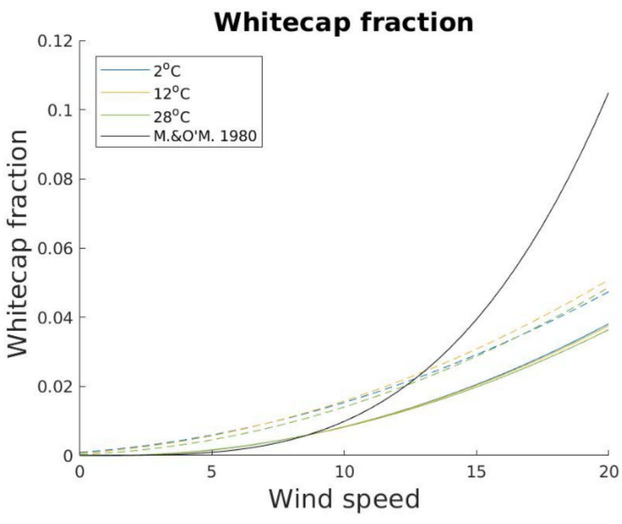


*Figure 24. Whitecap fraction parameterization. Black line is the Monahan & O'Muircheartaigh, colored lines are for the Albert et al. parametrization at three SST values. Solid lines for W10 and dashed lines for W37.*

## Testing the SSV improvements

Five different retrieval approaches with SDV were made, with different setups regarding the wind speed and white cap fraction (WCF) parameterization, as described in the Table below. In addition, MODIS/Terra retrieval was used for comparison. First, effect of changing the wind speed source in SSV from the previously used AEROCOM climatology to the ECMWF wind speed data included in the SLSTR L1B files was tested. Naturally the different wind speed values cause differences in AOD in some cases, but on the monthly average level the differences are small. Pixel per pixel correlation between SSV with AEROCOM and ECMWF wind speed is 0.95, and the average AOD remains the same at 0.18. In fact, the comparisons between all approaches employed in this exercise show similarly small differences on monthly level. Comparison with MODIS gives the same correlation coefficient for all SDV approaches. Figure 25 shows scatter plots of AOD comparison between MODIS and two SDV data sets with different white cap fraction parameterizations.

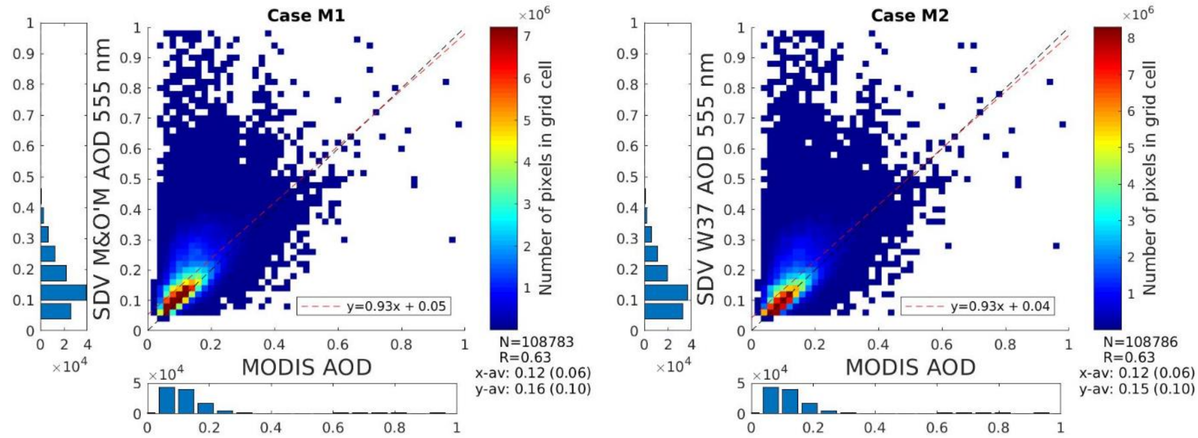


*Figure 25 Comparison of MODIS and SDV AODs for two WCF parameterizations.*

Figure 26 shows two examples of the comparison scatter plots for the one month data set. Large majority of data points show low AOD values. For larger AOD values the differences between the approaches are larger. Understanding these differences would require more detailed cases studies. Daily plots of AOD maps using different approaches did not reveal any obvious sources of discrepancy.

| Case abbreviation | Description | Mean AOD | Corr. wrt M&O'M | Corr. wrt MODIS |
|---|---|---|---|---|
| AEROCOM | Windspeed from AEROCOM climatology, WCF from M&O'M. | 0.18 | 0.95 | 0.63 |
| M&O'M | Windspeed from ECMWF NRT, WCF from M&O'M | 0.18 | - | 0.63 |
| NTC | Windspeed from ECMWF NTC, WCF from M&O'M | 0.18 | 0.95 | 0.63 |
| AlbW10 | Windspeed from ECMWF NRT, WCF from Albert et al. (W10 parameters). | 0.18 | 0.95 | 0.63 |
| AlbW37 | Windspeed from ECMWF NRT, WCF from Albert et al. (W37 parameters). | 0.17 | 0.95 | 0.63 |
| MODIS | MODIS/Terra retrieval. | 0.12 | 0.63 | |

*Table 5 Comparison of five SSV approaches and MODIS.*

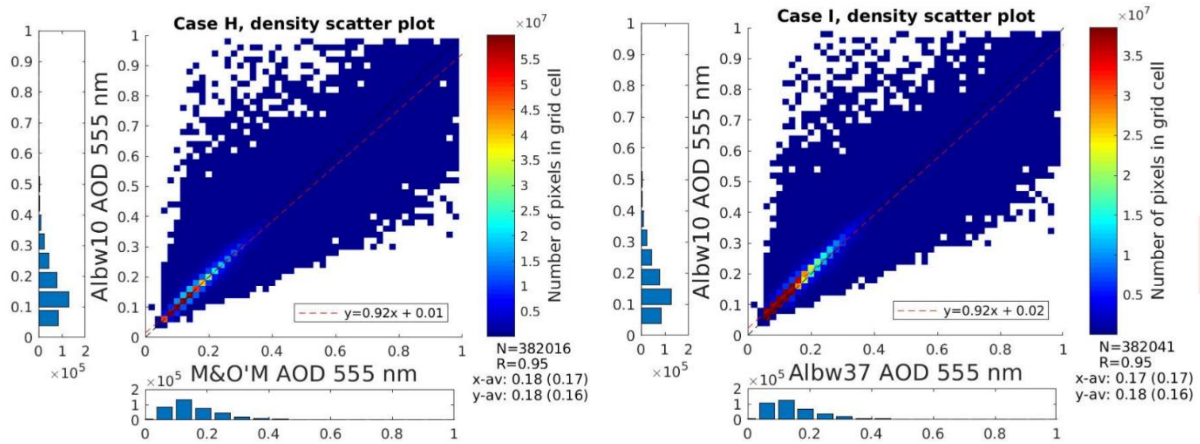


*Figure 26. Scatterplots of AOD retrieved with different whitecap fraction parameterizations.*

More differences between the WCF parametrizations used for SSV are revealed when we do the comparison using wind speed bins. Figure 27 shows the comparison between the old (M&O'M) and the new (AlbW37) parametrizations for four wind speed (u) bins: u < 5; 5 < u < 10; 10 < u <15; and 15 < u < 20 [m/s]. We see that for the low wind speeds the AOD is lower for the new parametrization, while for the higher wind speeds it becomes higher. This is in agreement with the white cap fraction shown in Figure 24: a lower WCF means that larger part of the measured TOA reflectance comes from the aerosols, leading to higher AOD value in the retrievals.

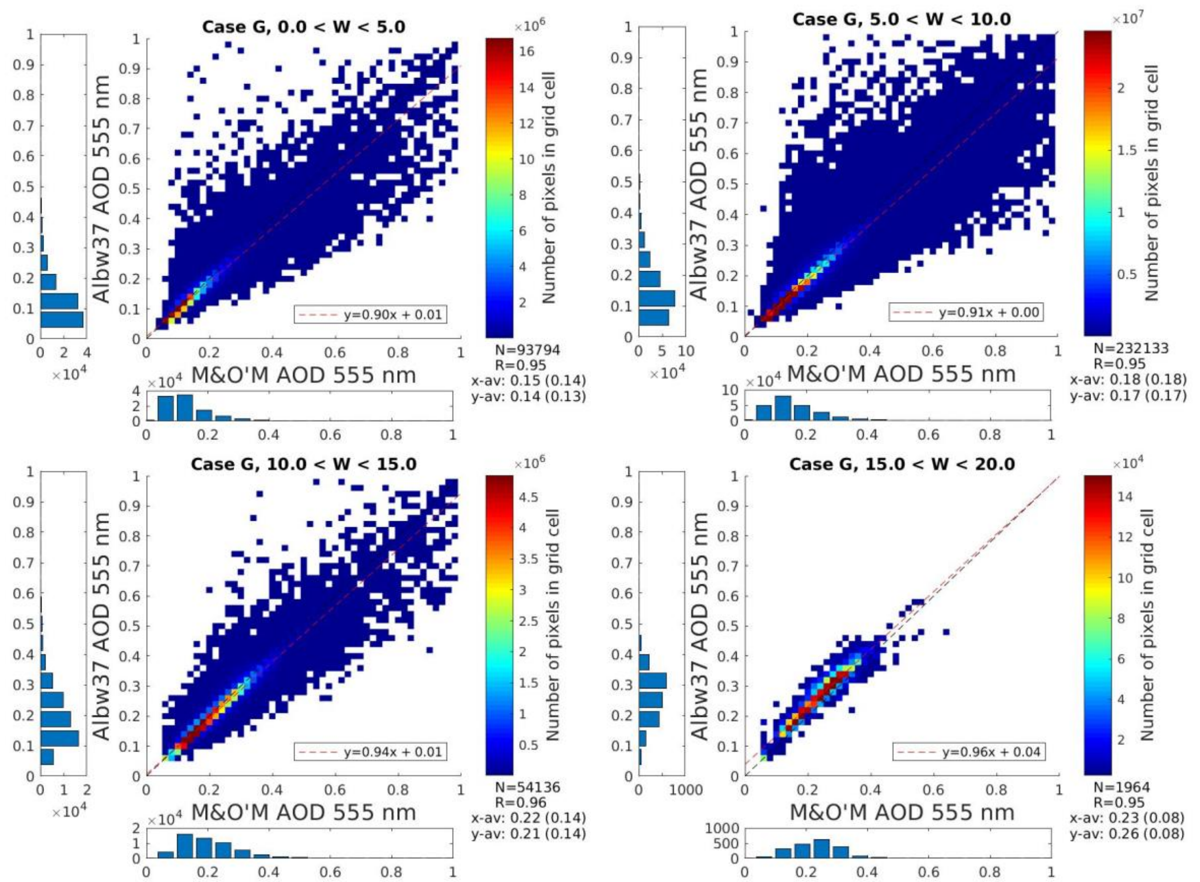


*Figure 27 SSV approach comparison with wind speed bins.*

# Conclusions

This SARP option project was the continuation of the main project reported in [D-1] and [D-2]. In the end of the main project it was concluded that specific retrieval geometries of the dual-view SLSTR instrument were causing poor performance. This was observed in retrievals with simulated and measured TOA reflectance. One of the recommendations was to test whether for the k-ratio, which is a crucial part the core SDV algorithm, spectral constraints could be determined to enhance the retrieval performance.

A basic test was done for spectral constraint for k-ratio of setting the ratio for each wavelength from the known surface in the simulations. This, in principle, should have led to accurate AOD but the results did not actually improve from the results of the baseline SDV algorithm with spectrally constant k-ratio assumption. Towards the end of the project, it was understood that the implicit assumptions made in the SDV retrieval render the direct application of the spectral k-ratio values inefficient in improving the retrieval performance. With the simulated data, the effect of the different assumptions made in SDV formalism can now be studied in detail, allowing development of more sophisticated spectral constraints in the future. A different kind of spectrally constrained method was developed instead where k-ratios determined at 1610 nm and 555 nm are combined and then linked to AOD. The method was tested at a proof-of-concept level using simulations.

Second part of the project was the continuation of the testing of the SLSTR calibration correction with the new (introduced in year 2020) corrections.

When the inverse of new corrections was applied to the simulated data as calibration errors it was observed that where the SDV algorithm over land has poor performance due to challenging retrieval geometry, the AOD error caused by calibration error was large. In geometries where the SDV algorithm works well the calibration has a rather small effect on the retrieved AOD; the algorithm is quite robust in taking advantage of the dual-view property of the SLSTR instrument. In addition, it was estimated based on the simulations that the error in TOA reflectance should be no more than 25% (P=0.25) of the inverse of the current calibration coefficients, to constrain the error in the retrieved AOD to be less than 100%. This corresponds to maximum tolerable error of 0.5% – 2.75% depending on the view and channel (Table 3). The estimate, however, depends on the retrieval geometry.

When the new calibration correction was applied to the actual S3A SLSTR L1b data, a large decrease in the retrieved AOD was observed especially over land in the Northern Hemisphere (average decrease of about 0.11) where the challenging retrieval geometries are dominant. The results look more sensible with the correction and the AERONET validation is improved. Over ocean a small decrease in the retrieved AOD was observed (0.005).

A new whitecap fraction parametrization was implemented and tested for SLSTR Single View (SSV) retrieval over ocean. The new parametrization leads to higher whitecap fraction and slightly lower AOD for low wind speeds (-0.01 decrease in AOD for $0 < w < 5$ m/s), and lower whitecap fraction and slightly higher AOD for high wind speeds (+0.03 increase in AOD for $15 < w < 20$ m/s), but on average the changes are very small (-0.01 decrease).

## References

Albert, M.F.M.A., Anguelova, M.D., Manders, A.M.M., Schaap, M., and de Leeuw, G., Parameterization of oceanic whitecap fraction based on satellite observations, Atmos. Chem. Phys., 16, 13725-13751, 2016.

Baker, K.S., and Smith, R.C., Bio-optical classification and model of natural waters 2, Limnol. Oceanogr., 27(3), 500-509, 1982.

Cox, C., W. Munk, Measurement of the roughness of the sea surface from photographs of the Sun's glitter, J. Opt. Soc. Am., 44, 838-850, 1954.

Feldman, G., Kuring, N., Ng, C., Esaias, W., McClain, C., Elrod, J., Maynard, N., Endres, D., Evans, R., Brown, J., Walsh, S., Carle, and M., Podesta, G., Ocean color: Availability of the global data set, Eos Trans. AGU, 70( 23), 634-641, doi:10.1029/89EO00184, 1989.

Flowerdew, R.J. and Haigh, J.D., An approximation to improve accuracy in the derivation of surface reflectances from multi-look satellite radiometers. Geophys. Res. Lett., 22, 1693--1696, 1995.

Gordon, H.R., Brown, O.B., Evans, R.H., Brown, J.W., Smith, R.C., Baker, K., and Clark, D.K., A Semianalytic Radiance Model of Ocean Color, J. Geophys. Res., 93, 10909-10924, 1988.

Ivanov, A. P., Physical Properties of Hydro-optics, Nauka i Tekhnika, Minsk, 1975.

Koepke, P., Effective reflectance of oceanic whitecaps, Applied Optics Vol. 23, 11, 1816-1824, doi:10.1364/AO.23.001816, 1984.

Monahan, E.C. and O'Muircheartaigh, I., Optimal power-law description of oceanic whitecap coverage dependence on wind speed, J. Phys. Ocean., 10, 2094-2099, 1980.

Morel, A., Optical modeling of the upper ocean in relation to its biogeneous matter content (case I waters), J. Geophys. Res., 93, 10749-10768, 1988.

Smith D., Assessment of Visible and Short Wavelength Radiometric Calibration using Vicarious Calibration Methods, Sentinel-3 MPC project document - S3MPC.RAL.TN.010, 2020.

Veefkind, J.P., de Leeuw, G., A new algorithm to determine the spectral aerosol optical depth from satellite radiometer measurements, J. Aerosol Sci., 29, 1237-1248, 1998.

Veefkind, J.P., de Leeuw, G.D., Stammes, P., and Koelemeijer, R.B.A., Regional distribution of aerosol over land, derived from ATSR-2 and GOME. Remote Sens. Environ., 74, 377--386 2000.

Wanner, W., Strahler, A.H., Hu, B., Lewis, P., Muller, J.-P., Li, X., Barker Schaaf, C.L., and Barnsley, M.J., Global retrieval of bidirectional reflectance and albedo over land from EOS MODIS and MISR data: theory and algorithm. J. Geophys. Res., 102, 17143--17161, 1997.

WMO, GCOS-200, THE GLOBAL OBSERVINGSYSTEM FOR CLIMATE:IMPLEMENTATION NEEDS, World Meteorological Organization, https://library.wmo.int/opac/doc_num.php?explnum_id=3417 (last accessed 18.3.2021), 2016.

# Appendix: Simulation studies related to the geometrical issues of the retrieval

## Relevant details of the SDV dual-view algorithm

In the algorithm the modeled TOA reflectance is of the form (Veefkind et al., 2000)

$$\rho(\mu_1,\mu,\phi,\lambda)=\rho_a(\mu_1,\mu,\phi,\lambda)+\frac{T(\mu_1,\mu,\phi,\lambda)\rho_s(\mu_1,\mu,\phi,\lambda)}{1-s(\lambda)R_s(\lambda)}, \qquad \text{(A.1)}$$

where $\rho_a$is the reflectance due to the atmosphere, $\rho_s$is the surface reflectance, $T$is the product of downward and upward atmospheric transmittance, $s$ is the spherical albedo (or the atmospheric backscatter ratio), and $R_s$ is the surface albedo. Reflectance and transmittance parameters: $\mu_1$ is the solar zenith angle, $\mu$ is the viewing (satellite) zenith angle, $\phi$ is the relative azimuth angle between the sun and the satellite, and $\lambda$ is the wavelength. Note that multiple scattering between surface and atmosphere is assumed here to be angle-independent for method development purposes. It has also been suggested that multiple scattering in the surface-atmosphere system will lead to isotropically distributed scattering (Wanner et al., 1997).

Possible problem with the assumption of isotropic surface albedo $R_s$ are evident. To this assumption to work, it must be assumed that either or both of the following conditions must be true.

- The value of the spherical albedo $s$ must be large enough for the isotropical multiple scattering.
- The surface reflectance is Lambertian to ensure the isotropic multiple scattering.

The dual-view method for AOD retrieval is derived based on the above assumptions. Equation (A.1) can be written separately for the nadir (n) and oblique (o) views. Then, by solving for the divisor $1-s(\lambda)R_s(\lambda)$ for both equations and combining **while keeping in mind that the multiple scattering is assumed to be angle independent**, relation

$$\frac{\rho^n(\mu_1,\mu,\phi,\lambda)-\rho_a^n(\mu_1,\mu,\phi,\lambda)}{\rho_s^n(\mu_1,\mu,\phi,\lambda)T^n(\mu_1,\mu,\phi,\lambda)}=\frac{\rho^o(\mu_1,\mu,\phi,\lambda)-\rho_a^o(\mu_1,\mu,\phi,\lambda)}{\rho_s^o(\mu_1,\mu,\phi,\lambda)T^o(\mu_1,\mu,\phi,\lambda)} \qquad \text{(A.2)}$$

can be formally made.

The nadir and oblique surface reflectance in equation (A.2) is replaced by the so-called *k*-ratio (Flowerdew and Haigh, 1995):

$$k=\frac{\rho_s^o(\mu_1,\mu,\phi,\lambda)}{\rho_s^n(\mu_1,\mu,\phi,\lambda)}. \qquad \text{(A.3)}$$

The ratio is assumed to be independent of the employed wavelengths. Assuming further that the effect of the atmospheric aerosols is generally low at infra-red, the *k*-ratio is determined utilizing the measured TOA reflectance at 1610 nm. Now equation (A.3) can be rewritten as

$$k=\frac{\rho^o(\mu_1,\mu,\phi,1610\ nm)}{\rho^n(\mu_1,\mu,\phi,1610\ nm)}. \qquad \text{(A.4)}$$

Now surface reflectance in equation (A.3) can be replaced by the *k*-ratio leading to the final retrieval formulation

$$\frac{\rho^n(\mu_1,\mu,\phi,\lambda)-\rho_a^n(\mu_1,\mu,\phi,\lambda)}{T^n(\mu_1,\mu,\phi,\lambda)}=\frac{\rho^o(\mu_1,\mu,\phi,\lambda)-\rho_a^o(\mu_1,\mu,\phi,\lambda)}{kT^o(\mu_1,\mu,\phi,\lambda)}. \qquad \text{(A.5)}$$

Of course, if the aerosol model and, thus, the atmospheric functions (reflectance, transmittance) are known and the corresponding measured reflectance is given, the *k*-ratio can be solved from the above equation:

$$k = \left[\frac{\rho^o(\mu_1,\mu,\phi,\lambda) - \rho_a^o(\mu_1,\mu,\phi,\lambda)}{T^o(\mu_1,\mu,\phi,\lambda)}\right]\left[\frac{\rho^n(\mu_1,\mu,\phi,\lambda) - \rho_a^n(\mu_1,\mu,\phi,\lambda)}{T^n(\mu_1,\mu,\phi,\lambda)}\right]^{-1}. \quad \text{(A.6)}$$

This equation can be used to observe what would be the k-ratio spectrum in simulations with perfect knowledge, and the spectrum can then be compared with the values given by equation (A.4).

## Implicit assumptions in SDV

The SDV forward model described by Eq. (A.1) is a simplification in that all direct and diffuse surface reflectance and atmospheric transmittance terms are bundled up to one term $T\rho$. This means that this surface reflectance term does not correspond to the direct surface reflectance (BRDF) term used in the simulations, but includes contributions from the diffuse surface reflectance terms. A more complete equation would be

$$\rho = \rho_a + \frac{T_\downarrow \rho_{s,dir} T_\uparrow + t_\downarrow \rho_{s,dif\downarrow} T_\uparrow + T_\downarrow \rho_{s,dif\uparrow} t_\uparrow + t_\downarrow \rho_{s,iso} t_\uparrow}{1 - sR_s} \quad \text{(A.7)}$$

where $T_\downarrow$ and $T_\uparrow$ are the direct downward and upward transmittance terms, $t_\downarrow$ and $t_\uparrow$ are the corresponding diffuse transmittance terms, $\rho_{s,dir}$ is the direct surface reflectance, $\rho_{s,dif\downarrow}$ describes the surface reflectance of diffuse downwelling radiation towards the satellite instrument, $\rho_{s,dif\uparrow}$ is the blac-sky albedo, and the isotropic term $\rho_{s,iso}$ is the white-sky albedo. By comparing with (A.1) we can nominally solve for the 'effective surface reflectance' term

$$\rho_s = \frac{T_\downarrow \rho_{s,dir} T_\uparrow + t_\downarrow \rho_{s,dif\downarrow} T_\uparrow + T_\downarrow \rho_{s,dif\uparrow} t_\uparrow + t_\downarrow \rho_{s,iso} t_\uparrow}{T_\downarrow T_\uparrow + t_\downarrow T_\uparrow + T_\downarrow t_\uparrow + t_\downarrow t_\uparrow}. \quad \text{(A.8)}$$

Figure 28 shows the different surface reflectance components (colored lines) for 555 nm and the effective surface reflectance (black line) as function of AOD and RAZ. Naturally, the real surface reflectance terms do not depend on the AOD level, but the effective surface reflectance does. Only the direct surface reflectance component depends on the relative azimuth angle; the effective surface reflectance is less sensitive to RAZ.

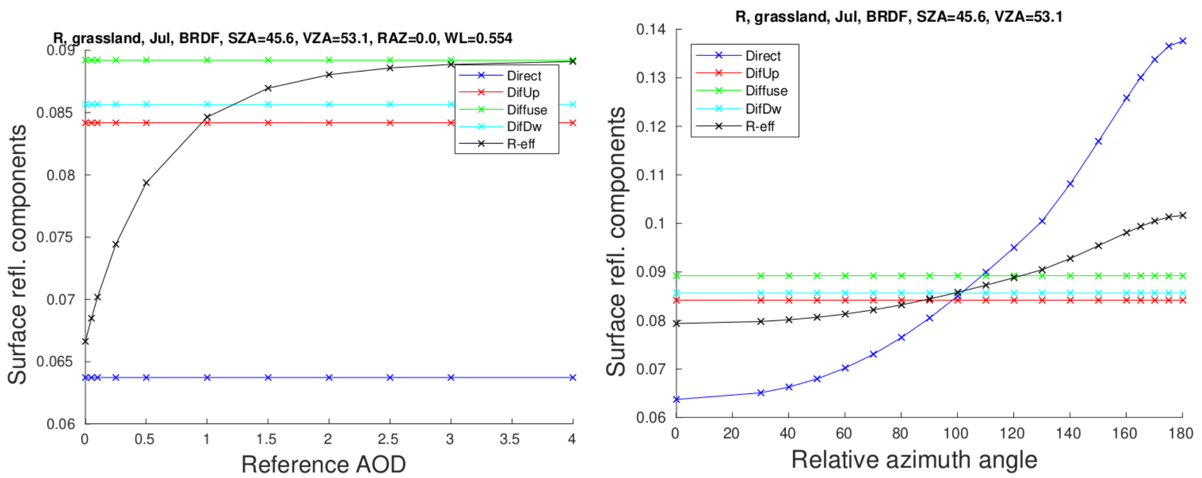


*Figure 28 Surface reflectance components from the simulations.*

With the simulations we can now consider how the different components affect the top of atmosphere reflectance, and what is the error caused by the simplification in the SDV forward model.

Figure 29 shows direct and diffuse surface reflectance components transmitted to the TOA level (red, green, cyan and magenta lines), the sum of these components corresponding to Eq. (A.7) (black line), the surface part from the simplified SDV forward model corresponding to Eq. (A.1), and the results from the full simulations $\rho - \rho_a$ (yellow line). We see that the error caused by the simplified SDV forward model to the surface signal (the difference between blue and yellow lines) is quite large, but the relative contribution to the total signal (including atmospheric reflectance) is smaller. We also see that for large RAZ there is difference between the full simulations (yellow line) and the sum of components (corresponding to Eq. (A.7), black line), which are presumably due to more accurate treatment of the multiple scattering effects in the libradtran simulations.

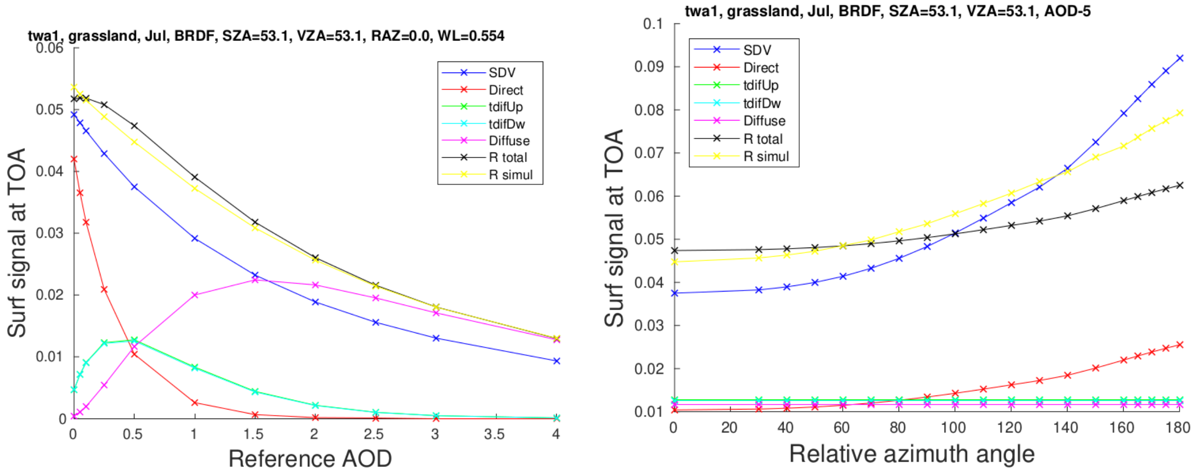


*Figure 29 Surface reflectance contribution to TOA reflectance with various approaches.*

Figure 30 shows the relative difference of the TOA reflectance between the simple SDV forward model and the full simulations in the oblique view for each wavelength as function of AOD and RAZ. Excluding 865 nm wavelength, which is not used in the retrieval, the worst errors are of order 5%. However, there are two things to take into account here. First, the surface contribution to TOA signal for individual views is not used as such in SDV; what is needed is the ratio of the reflectances in the two views, where the errors partly cancel. Secondly, in this comparison we have used the direct surface reflectance term $\rho_{s,dir}$ in place of $\rho_s$ in Eq. (A.1) when calculating the SDV TOA signal. This is done since the former term is available from the simulations, while the latter remains ambiguous. The comparison is not fair for SDV, since these two terms are not expected to be the same, as discussed above.

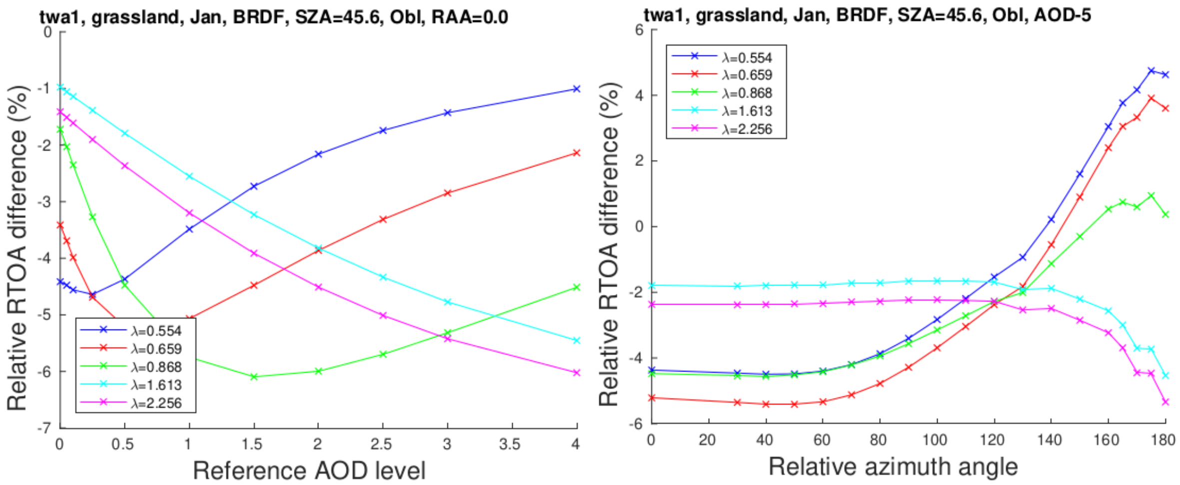


*Figure 30 Relative difference in TOA reflectance between SDV forward model and simulations.*

In order to illustrate the effect of SDV assumptions on ratio of reflectances, and to explain why the spectral k-ratio approach failed to improve SDV performance, we use the equation for the solved k-ratio (A.6). This equation does not give the "true" k-ratio, defined as the ratio of the surface reflectance components, but it can be understood as the form of k-ratio which is expected in the current SDV formalism. We use the solved k-ratio as a reference, and define the "error in k-ratio" by

$$E_k = \sum_{\lambda} [k_{solved}(\lambda) - k(\lambda)]^2$$

Figure 31 shows this "error" for the spectral k-ratio obtained from the modeled direct surface reflectance components respectively for each wavelength (k-spc, solid lines) and for the spectrally flat k-ratio obtained from the TOA reflectance at 1.6 (k-TOA, dashed lines). The colored lines show the individual spectral components (squared difference), and the black lines show the corresponding sum over wavelengths. We see that the "error" for k-TOA is generally larger and increases rapidly with increasing AOD, but for large RAZ the error for k-spc can be larger. It must be again emphasized that the solved k-ratio used as the reference here is not the "truth", but is derived from the simplified SDV forward model. Also, this "k-ratio error" does not describe the performance of the aerosol retrieval. The purpose of this figure is only to show the difference between the different k-ratio approaches, and to illustrate the difficulties in applying spectral constraints in the SDV formalism.

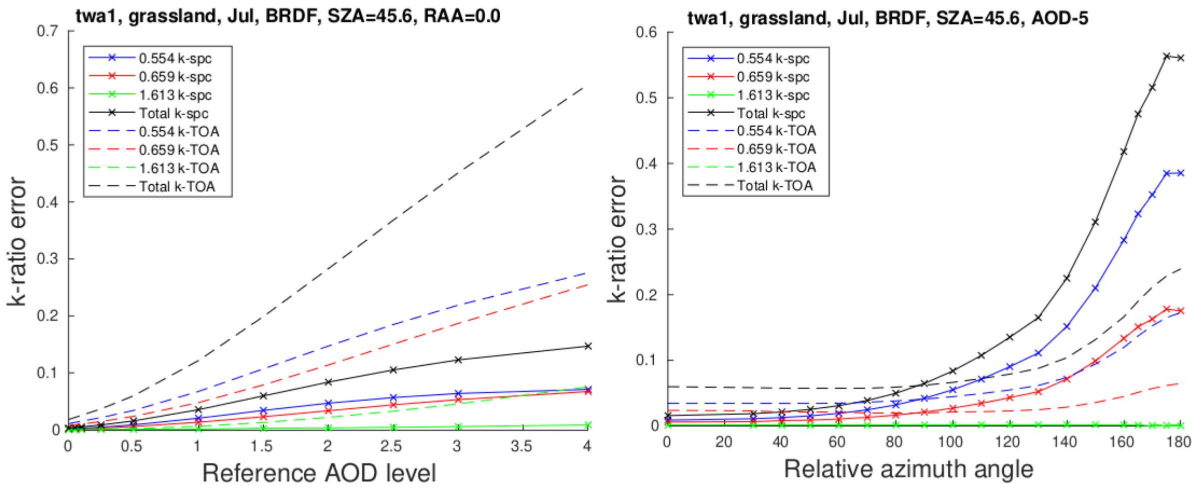


*Figure 31 Error in k-ratio as function of AOD and oblique view relative azimuth angle.*

## Addressing multiple scattering between surface and atmosphere in the *k*-ratio approach

In SDV the TOA reflectance is written in the form

$$\rho(\mu_0,\mu,\varphi,\lambda) = \rho_a(\mu_0,\mu,\varphi,\lambda) + \frac{T(\mu_0,\mu,\varphi,\lambda)\rho_g(\mu_0,\mu,\varphi,\lambda)}{1-s(\lambda)R_s(\lambda)}. \qquad \text{(A.9)}$$

This equation is an approximation. The direct and diffuse surface transmittance and reflectance are not treated respectively, but everything is bundled under the 'total transmittance' and the angle dependent surface reflectance term $\rho_g$. It is implicitly assumed that the direct transmittance/direct reflectance part dominates the TOA reflectance, and the terms including diffusive transmittance (scattering) are less significant. On the other hand, we are not trying to retrieve the direct and diffuse surface reflectance components in SDV, but the atmospheric part $\rho_a$. The surface reflectance term $\rho_g$ can be an effective term including both direct and diffusive components.

The multiple scattering is assumed to be isotropic, and hence albedos are used in the geometric sum term $1-s(\lambda)R_s(\lambda)$. Due to the diffuse nature of the multiple scattering, this is a reasonable assumption. However, our simulations suggest that there might be an implicit Lambertian assumption in SDV that affects its performance for large azimuth angles. Therefore, and alternative formulation was derived.

Some assumptions for the TOA reflectance are necessary for the dual view k-ratio method to be technically applicable. It is not possible to eliminate the surface reflectance terms from the dual view equations if both direct and diffuse surface reflectance are included. However, it is technically feasible to replace the isotropic surface albedo term $R_s$ with bi-directional reflectance. The reasoning is that despite the diffusive nature of the multiple scattering, the specular reflectance direction can be emphasized.

Technically, the treatment is as follows. We replace the isotropic surface albedo $R_s$ by angle dependent terms $R_s^N$ and $R_s^O$ for nadir and oblique view respectively. Then, we assume that these parameters are related by a term k':

$$R_s^O / R_s^N = k' \Rightarrow R_s^O = R_s^N (1 + (k' - 1)). \tag{A.10}$$

From the TOA reflectance equation, we then get, respectively for both views,

$$\frac{T^N \rho_g^N}{\rho^N - \rho_a^N} = 1 - sR_s^N$$

$$\frac{T^O \rho_g^O}{\rho^O - \rho_a^O} = 1 - sR_s^O = 1 - sR_s^N + (1 - k')sR_s^N \tag{A.11}$$

We combine the equations by eliminating $1 - sR_s^N$ and divide by $\rho_g^N$ to get

$$\frac{T^N}{\rho^N - \rho_a^N} = k \frac{T^O}{\rho^O - \rho_a^O} - (1 - k')s \frac{R_s^N}{\rho_g^N} \approx k \frac{T^O}{\rho^O - \rho_a^O} - (1 - k)s. \tag{A.12}$$

In the last equation we have further assumed $R_s^N \approx \rho_g^N$ and $k' \approx k$ as a first guess. This equation is now identical with the usual SDV retrieval equation, except for the ‘correction term’ $(1-k)s$. We note that for Lambertian surface (k=1) the correction term vanishes. We also note that the correction depends on the wavelength via the spherical albedo *s*.

## Description of SLSTR Single View (SSV) retrieval over ocean

In the SSV retrieval the Top-Of-Atmosphere (TOA) reflectance for ocean surface is modeled as

$$\rho_{TOA} = \rho_a + T_{\downarrow}\rho_{s,dir} /(1 - S \times \rho_{s,dir}) T_{\uparrow} + t_{\downarrow}\rho_{s,dif\downarrow} T_{\uparrow} + T_{\downarrow}\rho_{s,dif\uparrow} t_{\uparrow} + t_{\downarrow}\rho_{s,iso} t_{\uparrow}$$

(a) (b) (c) (d) (e)

where $\rho_{TOA}$ is the top-of-the atmosphere reflectance, *S* is the spherical albedo, *T* is the direct transmittance and *t* is the diffuse transmittance upwards (↑) and downwards (↓) . The terms $\rho_{\mathrm{a}}$ and $\rho_s$ are the atmospheric and surface reflectance, respectively, and the other terms come from the ocean surface model which is described in next section. The multiple scattering between surface and atmosphere has been included only for direct down – direct up case as it becomes negligible when diffuse transmittance is applied. Note that geometric and wavelength dependencies in the equation are omitted for brevity. In SSV we use the nadir view only, and the four SLSTR channels: S1, S2, S3 and S5.

Explanation of the components in the equation:

(a) Reflectance due to scattering in the atmosphere by aerosols and molecules.

(b) Photons transmitted downward, reflected by the ocean surface, and transmitted up.

(c) Photons scattered along the downward path, reflected by the ocean surface, and transmitted up.

(d) Photons transmitted downward, reflected by the ocean surface, and scattered towards the satellite instrument.

(e) Photons scattered along the downward path, reflected by the ocean surface, and scattered towards the satellite instrument.

The ocean surface reflectance is modeled as the sum of specular (Fresnel) reflectance (Cox and Munk, 1954) and reflectance by subsurface scattering. The Fresnel part is described by the geometric situation while the subsurface scattering is a function of chlorophyll concentration. The surface reflectance is a sum of four components based on atmospheric transmittance, see Eq. (1). The reflectance in these components is given by:

$$\rho_{s,dir}(\mu_0, \mu, \phi, \lambda) = \rho_{glint}(\mu_0, \mu, \phi, \lambda) + \rho_{chl}(C, \lambda)$$

where $\rho_{glint}$ is the sun glint and $\rho_{chl}$ is the subsurface reflectance due to chlorophyll concentration C, and it is assumed here to be Lambertian (Veefkind and de Leeuw, 1998a). In practice the reflectance due to sun glint is not taken into account because pixels flagged as sun glint in the SLSTR L1B data are not used in the retrieval. The geometric situation is described by the cosine of the solar zenith angle $\mu_0$, the cosine of the viewing zenith angle μ, and the relative azimuth angle $\phi$. Reflectance depends on the wavelength $\lambda$. Subsurface reflectance is modeled after (Morel, 1988) for case I waters as

$$\rho_{s,diff\downarrow}(\mu_0, \mu, \phi, \lambda) = \rho_{Fresnel}(\mu_0) + \rho_{alb}(C, \lambda, u)$$

$$\rho_{s,diff\uparrow}(\mu_0, \mu, \phi, \lambda) = \rho_{Fresnel}(\mu) + \rho_{alb}(C, \lambda, u)$$

$$\rho_{s,iso}(\mu_0, \mu, \phi, \lambda) = 0.066 + \rho_{alb}(C, \lambda, u)$$

In these equations $\rho_{Fresnel}$ is the Fresnel reflectance, and the factor 0.066 has been adapted from (Ivanov, 1975). The possible error caused by the approximate value is minimal because the contribution of the last term to the TOA reflectance is small. The albedo term $\rho_{alb}$

$$\rho_{alb}(C,\lambda,u) = (1-W)\rho_{chl}(C,\lambda) + \rho_{whitecap}(u)$$

includes the water leaving reflectance due to chlorophyll $\rho_{chl}$, and the contribution of the whitecap reflectance $\rho_{whitecap}$ determined by the fraction of the ocean surface covered by whitecaps (*W*). The chlorophyll term is (Gordon et al. 1988)

$$\rho_{chl} = \pi(1-0.021)(1-0.043)(1.33)^{-2}0.11b/K,$$

Where (Morel 1988)

$$b = 0.5b_w + b_b$$
$$b_b = 0.30C^{0.62}\left[0.002 + 0.02(0.5 - 0.25\log_{10} C)555/\lambda\right]$$

Parameter K is (Baker and Smith 1983):

$$K = K_w + K_c$$
$$K_c = k_c C \exp\left\{-\left[k_c'\log_{10}(C/C_{0)}\right]^2\right\} + 0.001C^2.$$

The parameters $k_c$, $k_c'$, $K_w$ and $b_w$ depend on wavelength and are tabulated as in Baker and Smith (1982). The chlorophyll concentration data in SSV comes from the Coastal Zone Color Scanner (CZCS) data (Feldman et al. 1989).

The whitecap reflectance $\rho_{whitecap}$ is a product of the whitecap albedo $s_{whitecap}$ and the whitecap fraction W

$$\rho_{whitecap} = s_{whitecap}W$$

The whitecap albedo is a function of wavelength, starting from 0.22 at 200 nm and going to zero at longer wavelengths (Koepke, 1984). In the SSV product version the whitecap fraction *W* is a function of wind speed *u* (Monahan and O'Muircheartaigh, 1980[1]):

$$W = 3.84\times10^{-6} \times u^{\,3.41}$$

Another parameterization for the whitecap fraction was tested in SARP Option 1 (Albert et al. 2016):

$$W = a(T)\left[U_{10} + b(T)\right]^2$$
$$a(T) = a_0 + a_1T + a_2T^2$$
$$b(T) = b_0 + b_1T$$

For the parameters $a_0$, $a_1$, $a_2$, $b_0$, and $b_1$ two alternative sets of values are provided by Albert et al., obtained from satellite radar observations at different wavelengths; these are labeled $W_{10}$ and $W_{37}$.

[1] Monahan, E.C. and O'Muircheartaigh, I., Optimal power-law description of oceanic whitecap coverage dependence on wind speed, J. Phys. Ocean., 10, 2094–2099, 1980.

## Lambertian exercise

Here some results for the Lambertian surface are shown. The amplitude of the Lambertian surface reflectance is coming from the cropland surface data base. The *k*-ratio can be set here to be exactly unity because of the strict Lambertian setting. The spherical albedo of the atmosphere *s* is, by definition, independent of geometry. Thus, the *k*-ratio assumption in equation (A.5) is fulfilled in principle. Figure 32 to Figure 35 show the simulated measured TOA reflectance (raw) and reflectance where the Rayleigh scattering has been removed for both views and for the wavelengths of 555 and 1610 nm. The aerosol signal at 1610 nm is small for the Urban/Background aerosol model which consists almost completely of fine aerosol particles. There is, however, some variation in the reflectance curve where around 90 degrees the aerosol signal vanishes for the oblique relative azimuth angle in Figure 34. Also notable is that the nadir TOA reflectance shape (Figure 32) approaches a horizontal line with decreasing AOD. This is straightforward as the Lambertian surface reflectance is constant as a function of the retrieval geometry.

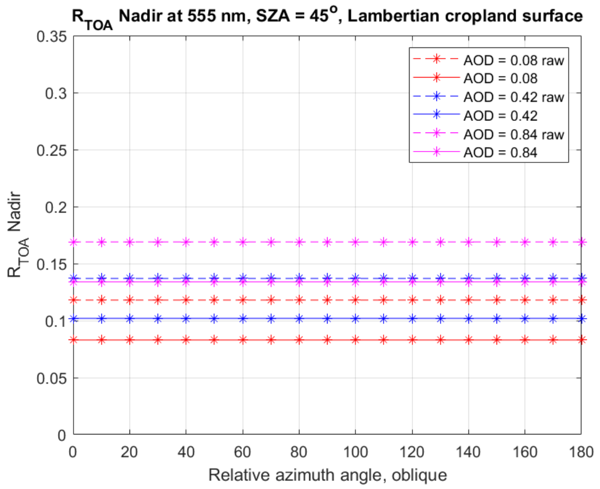


*Figure 32 Simulated **nadir** TOA reflectance at 555 nm for the Urban/Background aerosol type over the Lambertian cropland surface as a function of the relative azimuth angle of the oblique view. The term 'raw' refers here to the simulated TOA reflectance while the solid line indicates signal where the Rayleigh scattering has been removed.*

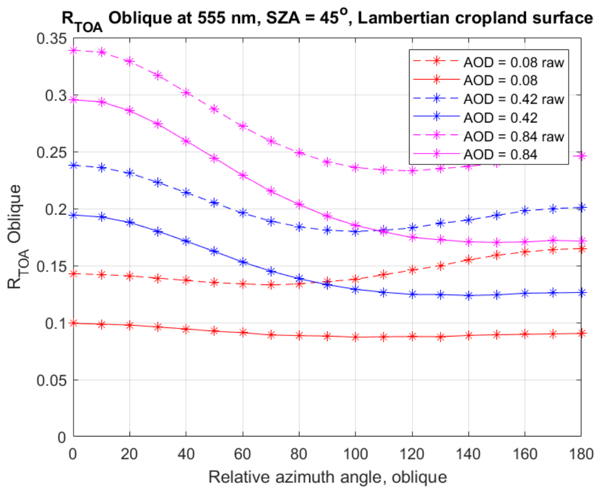


*Figure 33 Simulated **oblique** TOA reflectance at 555 nm for the Urban/Background aerosol type over the Lambertian cropland surface as a function of the relative azimuth angle of the oblique view. The term 'raw' refers here to the simulated TOA reflectance while the solid line indicates signal where the Rayleigh scattering has been removed.*

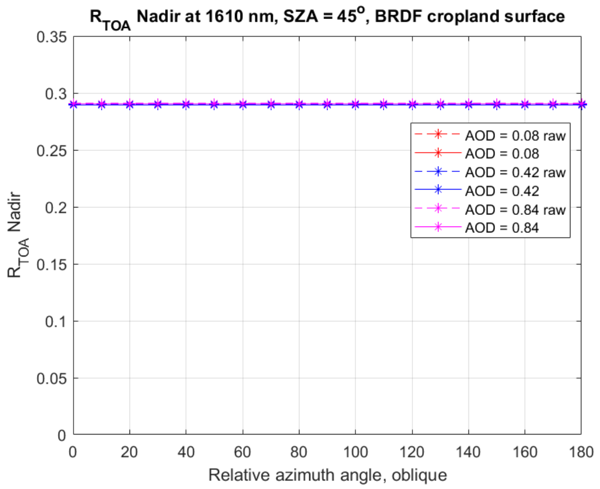


*Figure 34 Simulated **nadir** TOA reflectance at 1610 nm for the Urban/Background aerosol type over the Lambertian cropland surface as a function of the relative azimuth angle of the oblique view. The term 'raw' refers here to the simulated TOA reflectance while the solid line indicates signal where the Rayleigh scattering has been removed.*

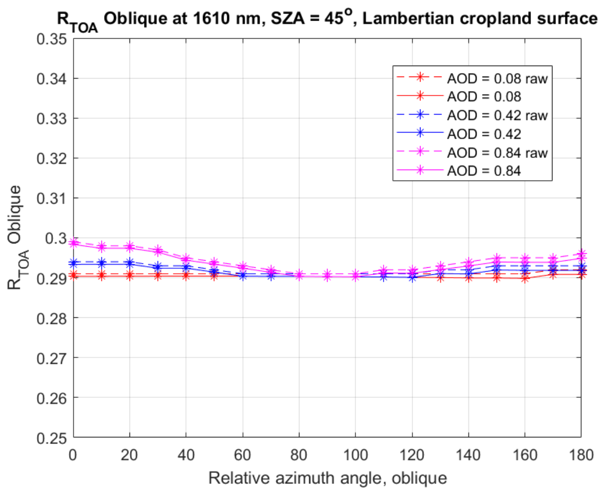


*Figure 35 Simulated **oblique** TOA reflectance at 1610 nm for the Urban/Background aerosol type over the Lambertian cropland surface as a function of the relative azimuth angle of the oblique view. The term 'raw' refers here to the simulated TOA reflectance while the solid line indicates signal where the Rayleigh scattering has been removed.*

Figure 36 shows the retrieved and reference AOD at 555 nm while Figure 37 shows the relative discrepancy between the retrieved and reference AOD values. The relative discrepancy seems to be a function of the oblique geometry, at least when the aerosol load is small. Figure 38 shows the retrieval results in detail for the reference AOD of 0.84 at 555 nm. The results give extended information about the retrieved aerosol model. The model is retrieved reasonably well but the small deviations from the reference values cannot be explained fully. The handling of the Rayleigh scattering may have a small contribution here. For this reason, the Rayleigh part of the retrieval algorithm was modified as explained later.

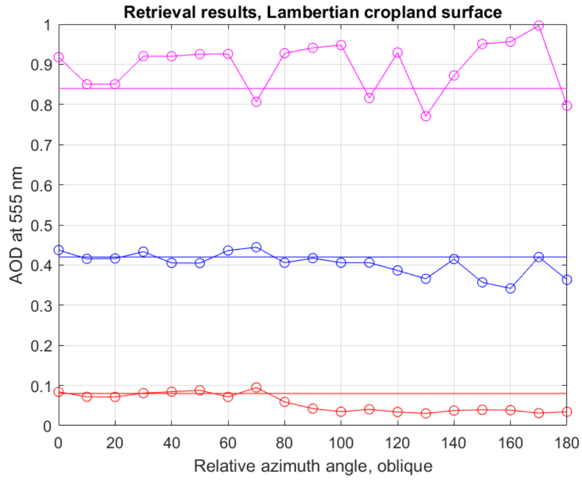


*Figure 36 AOD retrieval of the Urban/Background aerosol type over the Lambertian cropland surface as a function of the relative azimuth angle of the oblique view. Horizontal lines indicate the reference AOD values.*

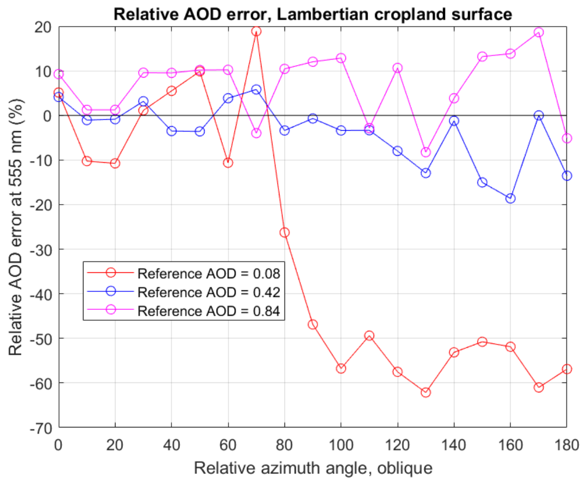


*Figure 37 Relative error in the AOD retrieval of the Urban/Background aerosol type over the Lambertian cropland surface as a function of the relative azimuth angle of the oblique view. Horizontal lines indicate the reference AOD values.*

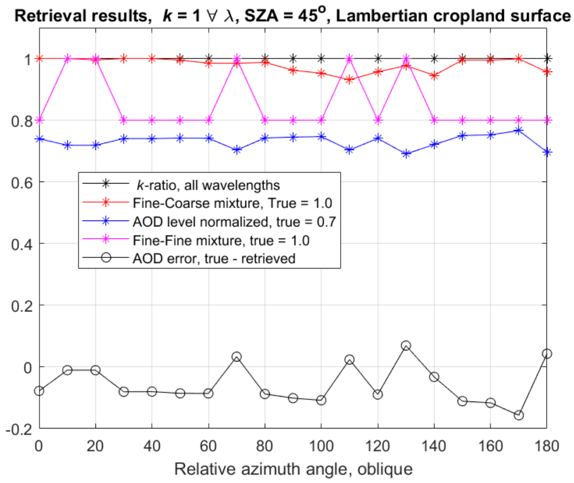


*Figure 38 Detailed information about AOD (0.84 at 555 nm) retrieval of the Urban/Background aerosol type over the Lambertian cropland surface as a function of the relative azimuth angle of the oblique view. The shown aerosol model parameters are the k-ratio, the mixture between the fine and coarse aerosol components, the mixture of the weakly and*

*strongly absorbing fine aerosol components, and the chosen AOD level in the LUTs (here normalized). In addition, the discrepancy between the retrieved and reference AOD is plotted.*

## BRDF exercise

Here the full BRDF results are shown for the same situation as for the Lambertian exercise. Here the *k*-ratio is determined with two distinct approaches:

1. **Product approach**: The *k*-ratio is determined by calculating the ratio using the TOA reflectance at 1610 nm. The Rayleigh scattering is subtracted first from the simulated measurement signal.
2. ***k*-spectral approach**: The *k*-ratio is determined from the simulated TOA reflectance where the AOD was set to the value of zero. The Rayleigh scattering has then been removed from the simulated TOA reflectance and the *k*-ratio computed for each wavelength separately. Equation (5) is applied by setting $k = k(\lambda)$, where $\lambda$ is 555, 659, or 1610 nm.

First, next four figures (Figure 39 - Figure 42) show the simulated TOA reflectance for the wavelengths of 555 and 1610 nm for nadir and oblique views. The third wavelength utilized in the aerosol retrieval (659 nm) is omitted here as the TOA reflectance behavior for this wavelength is like that of the 555 nm. The results of the retrieval are shown in Figure 43 for three reference AODs for both *k*-ratio approaches.

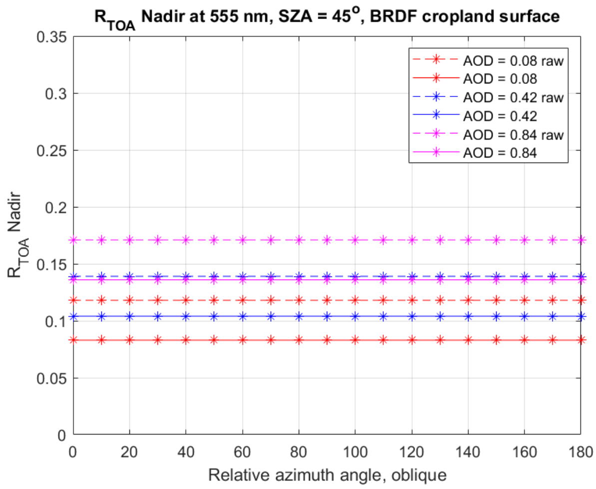


*Figure 39 Simulated **nadir** TOA reflectance at 555 nm for the Urban/Background aerosol type over the BRDF cropland surface as a function of the relative azimuth angle of the oblique view. The term 'raw' refers here to the simulated TOA reflectance while the solid line indicates signal where the Rayleigh scattering has been removed.*

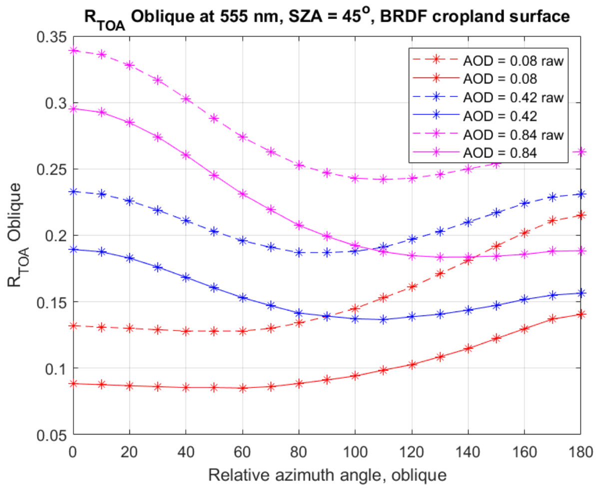


*Figure 40 Simulated **oblique** TOA reflectance at 555 nm for the Urban/Background aerosol type over the BRDF cropland surface as a function of the relative azimuth angle of the oblique view. The term 'raw' refers here to the simulated TOA reflectance while the solid line indicates signal where the Rayleigh scattering has been removed.*

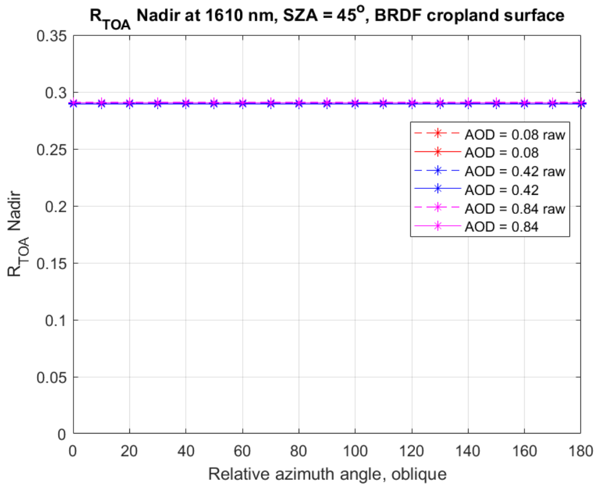


*Figure 41 Simulated **nadir** TOA reflectance at 1610 nm for the Urban/Background aerosol type over the BRDF cropland surface as a function of the relative azimuth angle of the oblique view. The term 'raw' refers here to the simulated TOA reflectance while the solid line indicates signal where the Rayleigh scattering has been removed.*

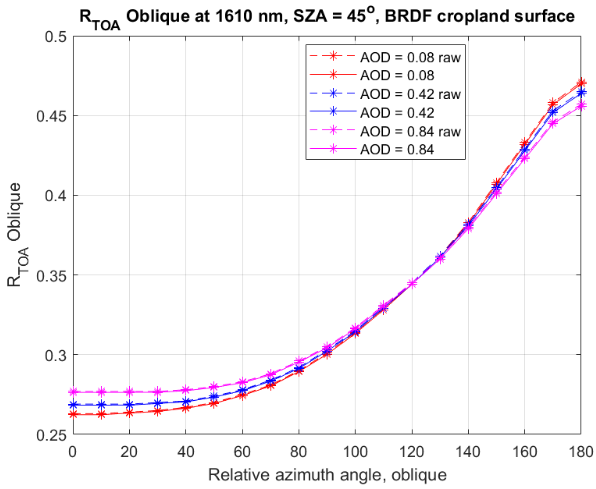


*Figure 42 Simulated* ***oblique*** *TOA reflectance at 1610 nm for the Urban/Background aerosol type over the BRDF cropland surface as a function of the relative azimuth angle of the oblique view. The term 'raw' refers here to the simulated TOA reflectance while the solid line indicates signal where the Rayleigh scattering has been removed.*

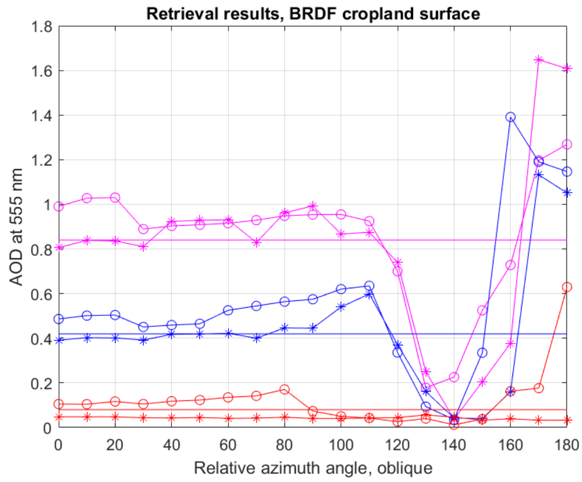


*Figure 43 AOD retrieval of the Urban/Background aerosol type over the BRDF cropland surface as a function of the relative azimuth angle of the oblique view. Horizontal lines indicate the reference AOD values. The circles mark the wavelength segregated k-ratio while the stars mark the k-ratio determined utilizing the 1610 nm TOA reflectance for the nadir and oblique views.*

Figure 44 shows the retrieval results in detail for the **product approach** for the reference AOD of 0.84 at 555 nm. The results give extended information about the retrieved aerosol model. It is obvious to see that there is now a connection between the quality of the retrieval and the TOA reflectance at 1610 nm. First, the aerosol signal seems to vanish nearly or almost completely when the oblique relative azimuth angle has values between 100 and 160 degrees. Second, there still seems to be problems with the AOD level parameter when the azimuth angle has values greater than 160 degrees even though there is a small but clear aerosol signal. The aerosol contribution has an opposite effect on the 1610 nm TOA reflectance to when the azimuth angle value is below 100 degrees. These TOA reflectance connections to the retrieval results seem not to be present at 555 nm although there is a substantial change in the aerosol signal amplitude toward larger values of the oblique relative azimuth angle. A notable observation is that the *k*-ratio value behaves smoothly throughout the azimuth angle space. More testing is needed to extract knowledge about its effect on the AOD retrieval.

Figure 45 shows the retrieval results in detail for the ***k*-spectral approach** for the reference AOD of 0.84 at 555 nm. The *k*-ratio is somewhat different at 555 nm to the one from the product approach (also plotted). Otherwise, the results seem to share mostly features with the results from the first approach. It is quite clear that the constraining the retrieval with some a priori knowledge about the actual *k*-ratio defined with actual surface reflectance is not enough to enhance the AOD retrieval performance. Other parallel or combined solutions must be sought.

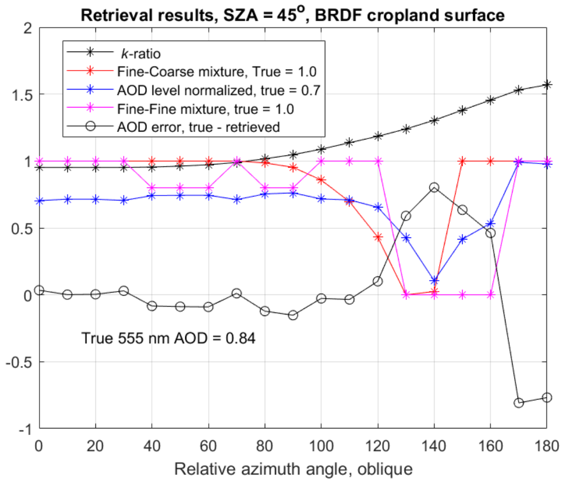


*Figure 44 **Product approach**. Detailed information about AOD (0.84 at 555 nm) retrieval of the Urban/Background aerosol type over the BRDF cropland surface as a function of the relative azimuth angle of the oblique view. The shown aerosol model parameters are the k-ratio, the mixture between the fine and coarse aerosol components, the mixture of the weakly and strongly absorbing fine aerosol components, and the chosen AOD level in the LUTs (here normalized). In addition, the discrepancy between the retrieved and reference AOD is plotted.*

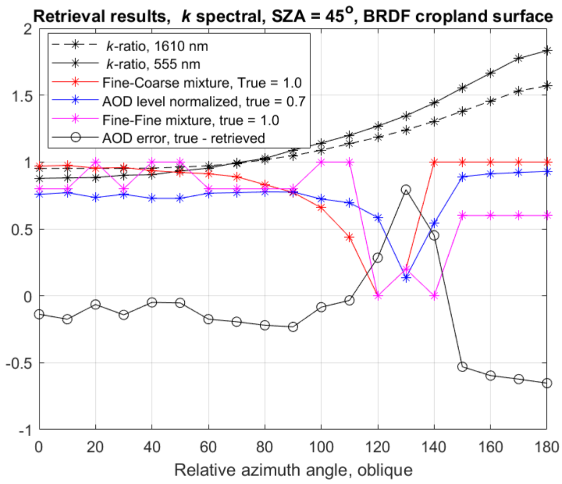


*Figure 45 **k-spectral approach**. Detailed information about AOD (0.84 at 555 nm) retrieval of the Urban/Background aerosol type over the BRDF cropland surface as a function of the relative azimuth angle of the oblique view. The shown aerosol model parameters are the k-ratio (for 555 nm as well as the product approach k-ratio at 1610 nm), the mixture between the fine and coarse aerosol components, the mixture of the weakly and strongly absorbing fine aerosol components, and the chosen AOD level in the LUTs (here normalized). In addition, the discrepancy between the retrieved and reference AOD is plotted.*

## Computation of the *k*-ratio with perfect knowledge

Here we exploit the simulations by using equation (A.6) and perfect knowledge about the aerosol model and loading to compute *k*-ratios to be compared with the *k*-ratio determined using the TOA reflectance at 1610 nm. The aerosol model here is of the Urban/Background type. Figure 46 and Figure 47 show the *k*-ratio comparison for AOD = 0.04 and AOD = 0.84 at 555 nm, respectively.

First thing to observe is that the *k*-ratio required to achieve the set AOD conditions behaves as a function of the AOD which is opposed to the assumptions. The *k*-ratio is the ratio of the oblique and nadir *surface* reflectance, and, thus, should not depend on any atmospheric conditions. There is a weak Lambertian assumption in the formal derivation of the retrieval equation (A.5). The multiple scattering between surface and atmosphere is assumed to be isotropic. This may be causing the observed behavior of the *k*-ratio as a function of the AOD. It is possible to formulate the retrieval function by replacing the surface albedo in equation (A.1) with anisotropic surface reflectance. The multiple scattering modified *k*-ratio treatment was explained above.

The second phenomenon to be pointed out in these results is that the *k*-ratios agree reasonably well when the relative azimuth angle of the oblique view has values less than about 100 degrees. The curious feature here is that the changes in the AOD are reflected obviously with the TOA reflectance determined *k*-ratio, but, on the other hand, these changes are reflected by the solved *k*-ratio.

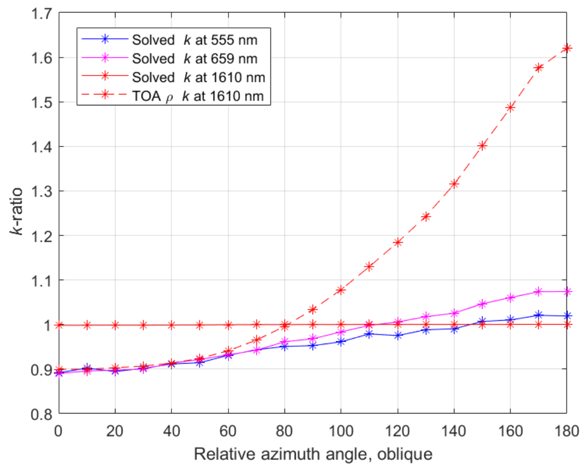


*Figure 46* ***AOD = 0.04 at 555 nm.*** *The k-ratio computed using equation (A.6) for the three wavelengths utilized in the aerosol retrieval (solid lines) and using TOA reflectance at 1610 nm (dashed line).*

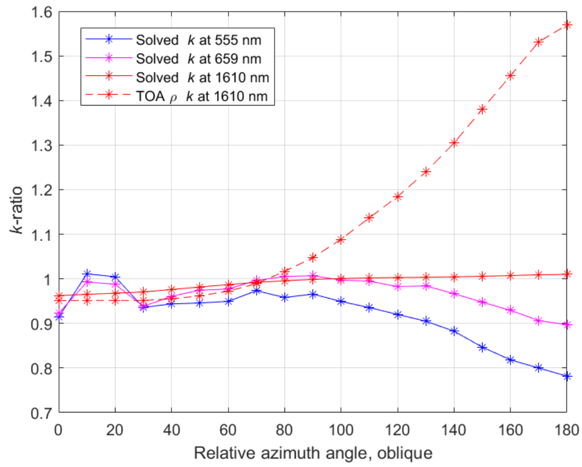


*Figure 47* ***AOD = 0.84 at 555 nm****. The k-ratio computed using equation (A.6) for the three wavelengths utilized in the aerosol retrieval (solid lines) and using TOA reflectance at 1610 nm (dashed line).*

## Note: Changes during the option project in the retrieval algorithm not related to surface treatment

During the investigation of the geometry related challenges in the aerosol retrieval using the SLSTR dual view feature it was noticed that there is some deficiency in the handling of the Rayleigh scattering. The retrieval algorithm has been implemented in such a way that the Rayleigh scattering is first excluded from the measured and modelled TOA reflectance. This exclusion was carried out by subtracting the Rayleigh reflectance from all TOA reflectance (measured and modelled). While the subtraction is a valid procedure from the point of view of TOA reflectance modelling, it does not consider multiple scattering between surface and atmospheric molecules. Now a divisive decision had to be made. Whether to exclude the Rayleigh scattering in a physically feasible way or run the retrieval process with the scattering included. After scrutiny of the SDV algorithm it was decided that the retrieval can be run without the extra handling of the Rayleigh scattering. In this approach the retrieval process is less "clean" in principle but there is the very advantageous benefit of a simpler algorithm. The simplicity was chosen to minimize the possibility of mishandling of the Rayleigh scattering.

# Appendix: The retrieval results of the full angle simulations

Here the AOD results of the retrievals using the full angle TOA simulations. Here “full angle” refers to simulations where also the viewing zenith angle was varied. In the results, the relative error (saturated to a range of -50% to 50% for easier comparison of the figures) with respect to the reference AOD values (indicated in the figures) is plotted as the function of nadir and oblique scattering angle. The results are plotted for the weakly scattering aerosol model, six land surfaces (cropland, desert, forest, grassland, urban, sparse vegetation; see [D-1] and [D-2]), and four months (January, April, July, October). Additionally, for completeness sake, some retrieval geometry angles are plotted as functions of the nadir and oblique scattering angles. In these figures SZA = sun zenith angle, VZA = viewing zenith angle, RAZ = relative azimuth angle. Note that the sun zenith angle is the same for the nadir and oblique view; the small time-difference between the scans is considered here to be negligible.

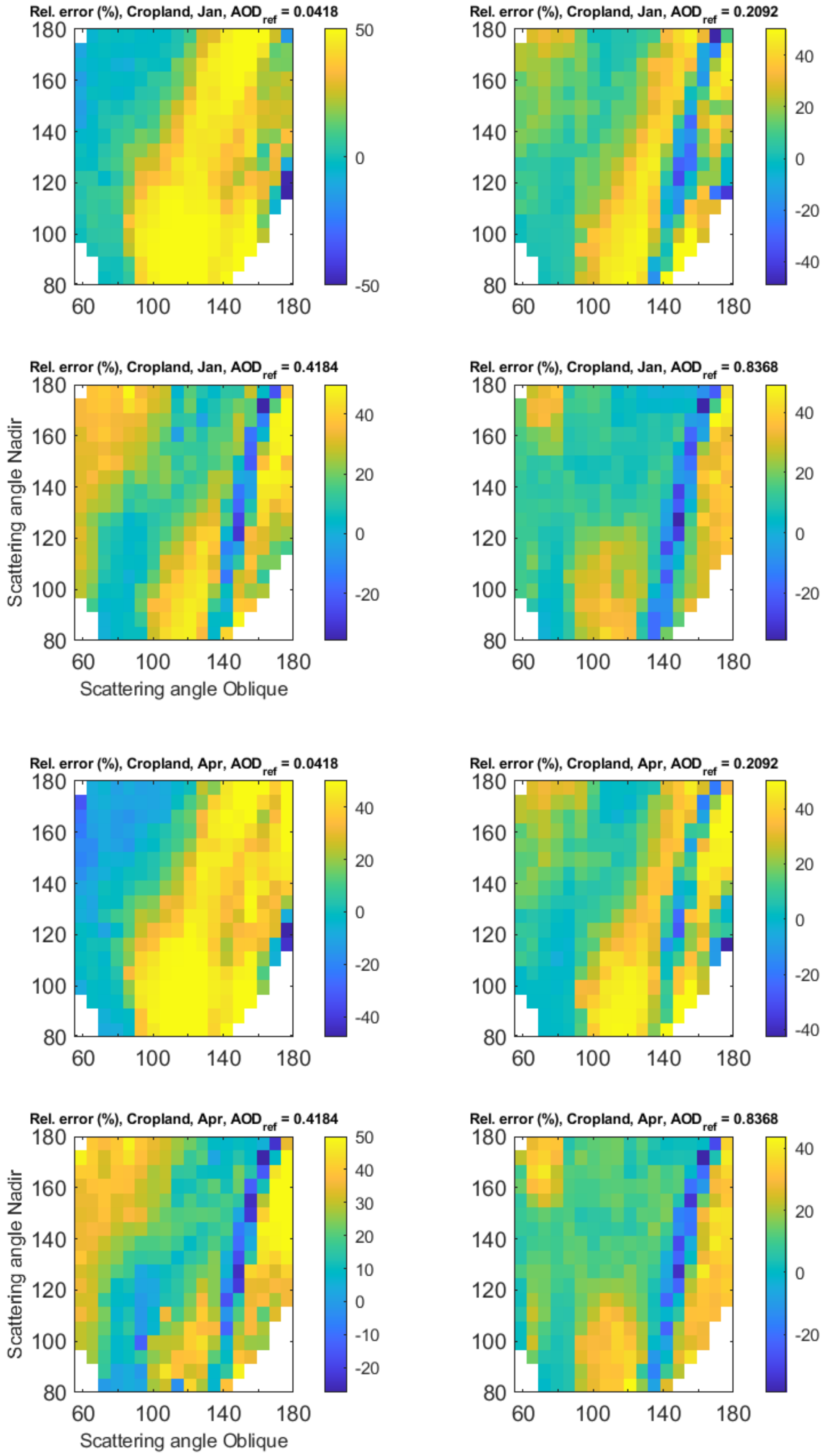

Rel. error (%), Cropland, Jan, AOD$_{ref}$ = 0.0418
Rel. error (%), Cropland, Jan, AOD$_{ref}$ = 0.2092
Rel. error (%), Cropland, Jan, AOD$_{ref}$ = 0.4184
Rel. error (%), Cropland, Jan, AOD$_{ref}$ = 0.8368
Rel. error (%), Cropland, Apr, AOD$_{ref}$ = 0.0418
Rel. error (%), Cropland, Apr, AOD$_{ref}$ = 0.2092
Rel. error (%), Cropland, Apr, AOD$_{ref}$ = 0.4184
Rel. error (%), Cropland, Apr, AOD$_{ref}$ = 0.8368
Scattering angle Nadir
Scattering angle Oblique

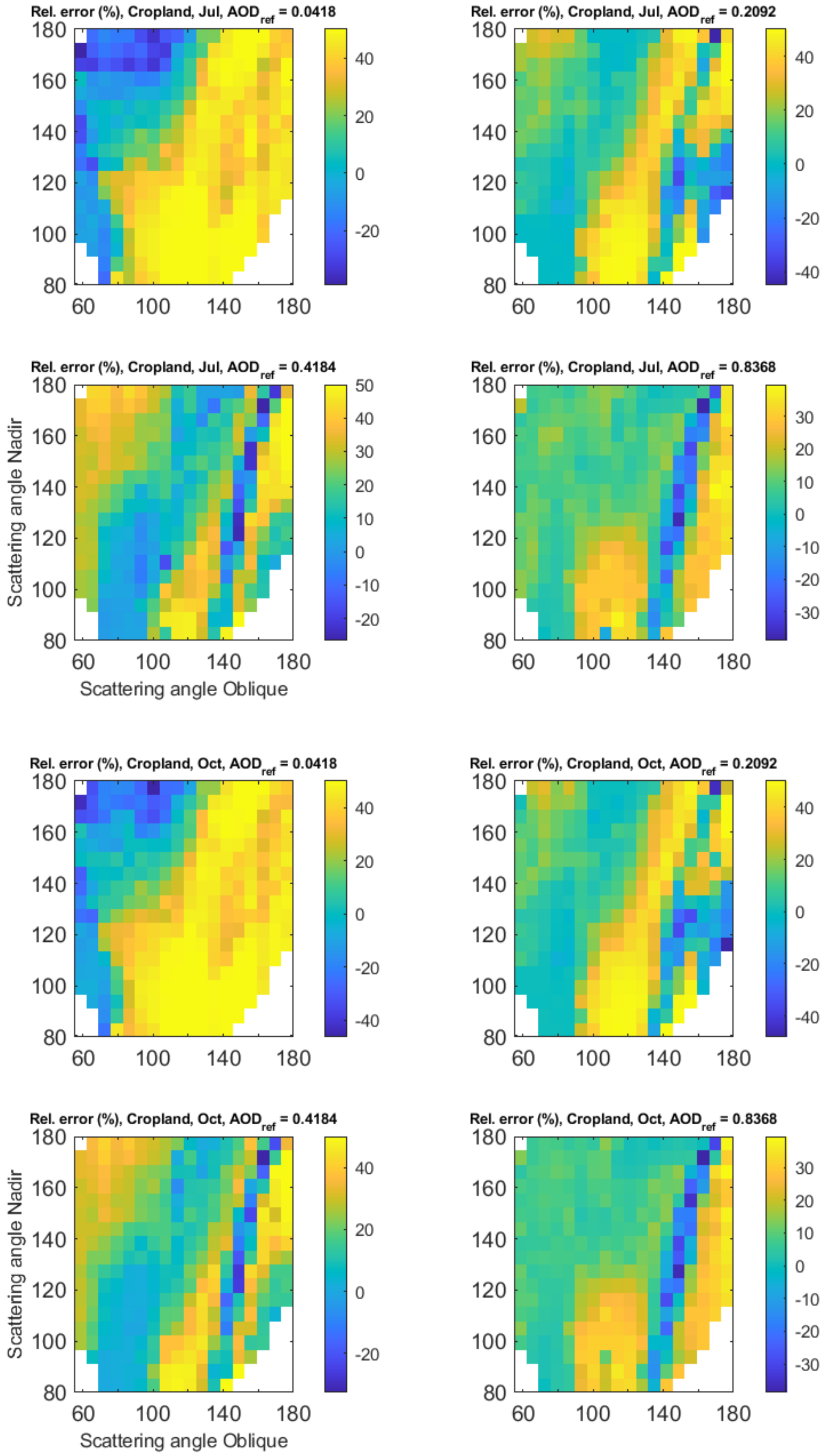
Rel. error (%), Cropland, Jul, $AOD_{ref}$ = 0.0418
Rel. error (%), Cropland, Jul, $AOD_{ref}$ = 0.2092
Rel. error (%), Cropland, Jul, $AOD_{ref}$ = 0.4184
Rel. error (%), Cropland, Jul, $AOD_{ref}$ = 0.8368
Rel. error (%), Cropland, Oct, $AOD_{ref}$ = 0.0418
Rel. error (%), Cropland, Oct, $AOD_{ref}$ = 0.2092
Rel. error (%), Cropland, Oct, $AOD_{ref}$ = 0.4184
Rel. error (%), Cropland, Oct, $AOD_{ref}$ = 0.8368
Scattering angle Nadir
Scattering angle Oblique

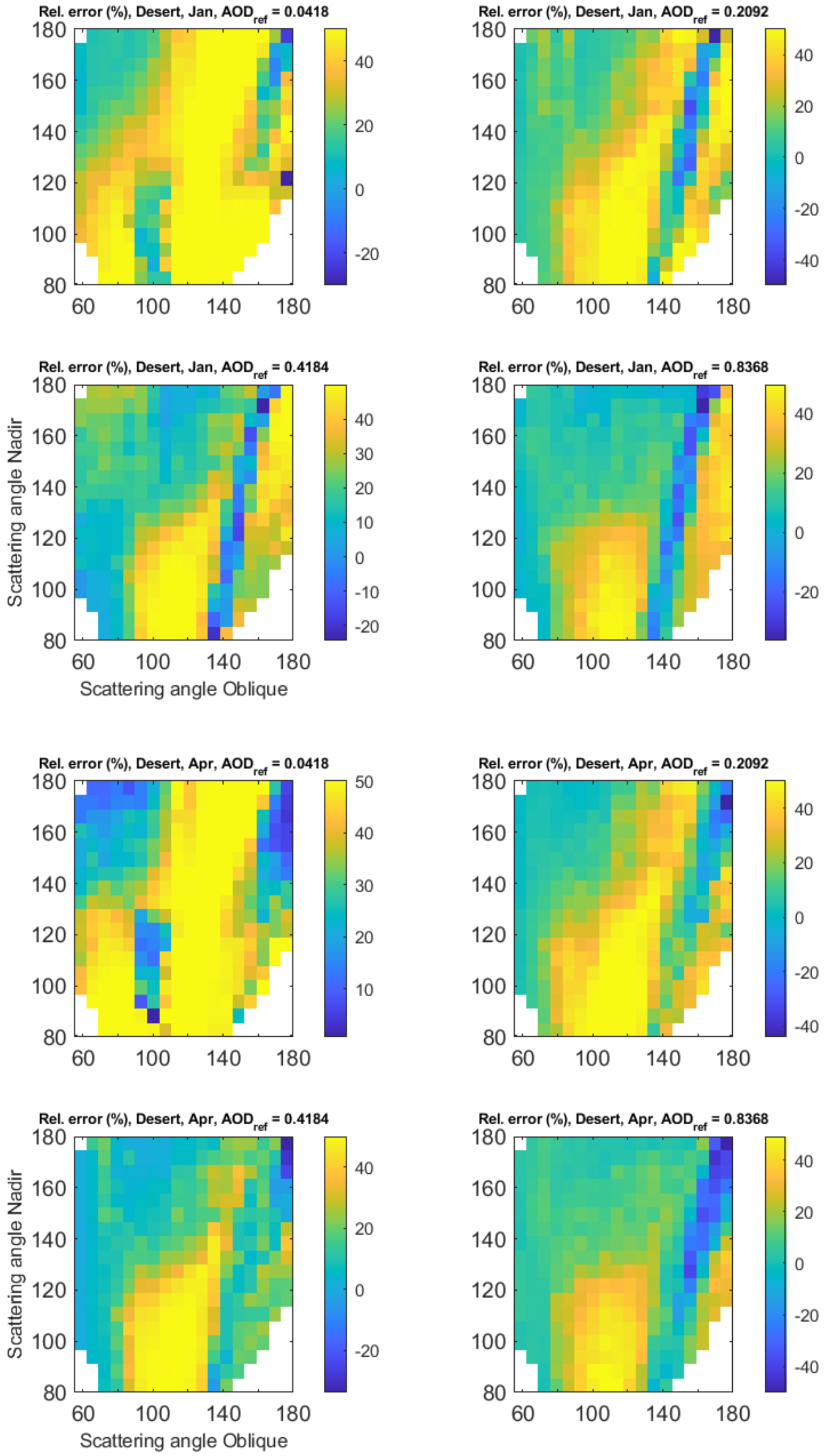
Rel. error (%), Desert, Jan, $AOD_{ref}$ = 0.0418
Rel. error (%), Desert, Jan, $AOD_{ref}$ = 0.2092
Rel. error (%), Desert, Jan, $AOD_{ref}$ = 0.4184
Rel. error (%), Desert, Jan, $AOD_{ref}$ = 0.8368
Rel. error (%), Desert, Apr, $AOD_{ref}$ = 0.0418
Rel. error (%), Desert, Apr, $AOD_{ref}$ = 0.2092
Rel. error (%), Desert, Apr, $AOD_{ref}$ = 0.4184
Rel. error (%), Desert, Apr, $AOD_{ref}$ = 0.8368
Scattering angle Nadir
Scattering angle Oblique

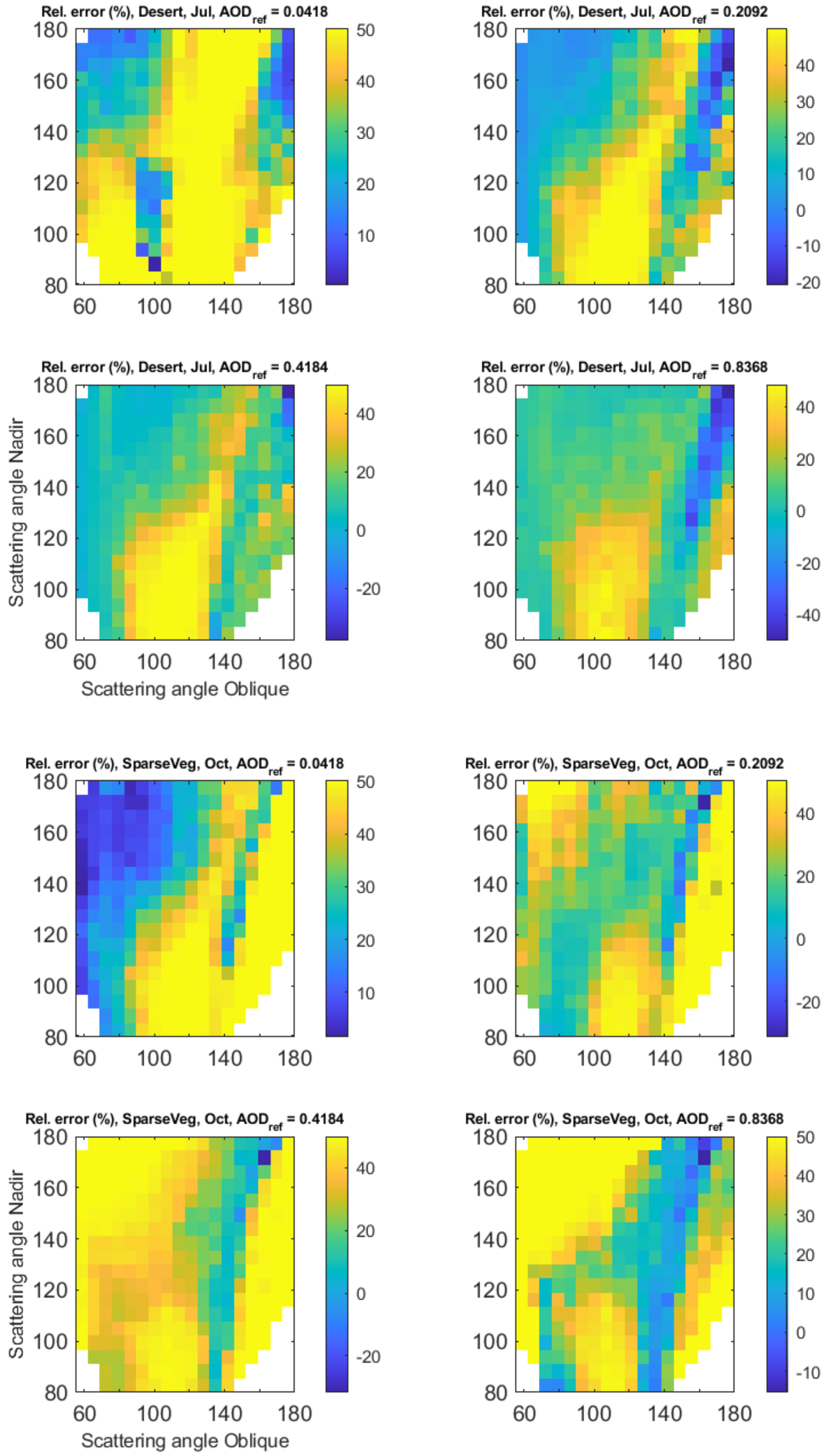

Rel. error (%), Desert, Jul, AOD_ref = 0.0418
Rel. error (%), Desert, Jul, AOD_ref = 0.2092
Rel. error (%), Desert, Jul, AOD_ref = 0.4184
Rel. error (%), Desert, Jul, AOD_ref = 0.8368
Scattering angle Nadir
Scattering angle Oblique
Rel. error (%), SparseVeg, Oct, AOD_ref = 0.0418
Rel. error (%), SparseVeg, Oct, AOD_ref = 0.2092
Rel. error (%), SparseVeg, Oct, AOD_ref = 0.4184
Rel. error (%), SparseVeg, Oct, AOD_ref = 0.8368
Scattering angle Nadir
Scattering angle Oblique

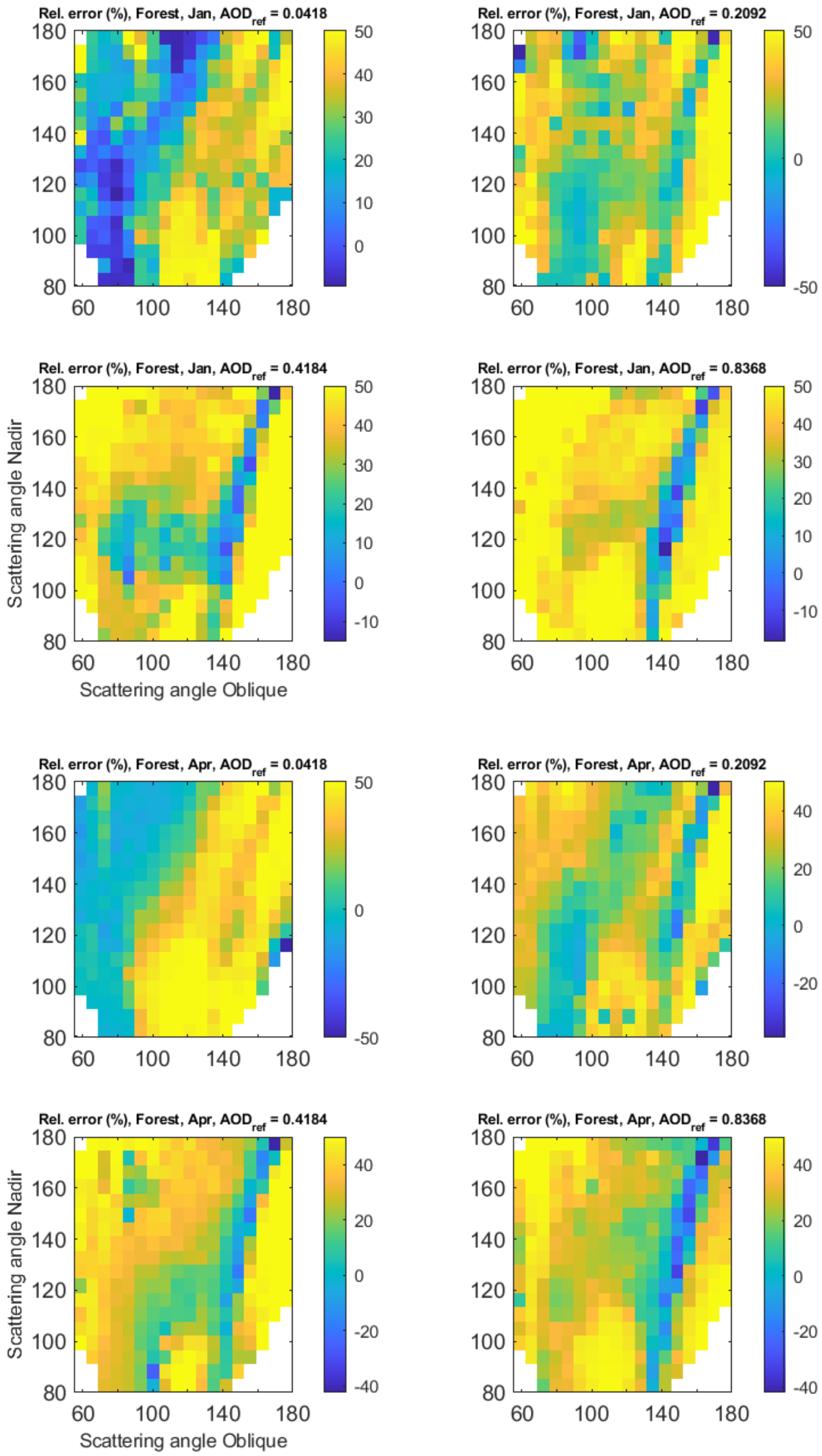

Rel. error (%), Forest, Jan, $AOD_{ref}$ = 0.0418
Rel. error (%), Forest, Jan, $AOD_{ref}$ = 0.2092
Rel. error (%), Forest, Jan, $AOD_{ref}$ = 0.4184
Rel. error (%), Forest, Jan, $AOD_{ref}$ = 0.8368
Rel. error (%), Forest, Apr, $AOD_{ref}$ = 0.0418
Rel. error (%), Forest, Apr, $AOD_{ref}$ = 0.2092
Rel. error (%), Forest, Apr, $AOD_{ref}$ = 0.4184
Rel. error (%), Forest, Apr, $AOD_{ref}$ = 0.8368
Scattering angle Nadir
Scattering angle Oblique

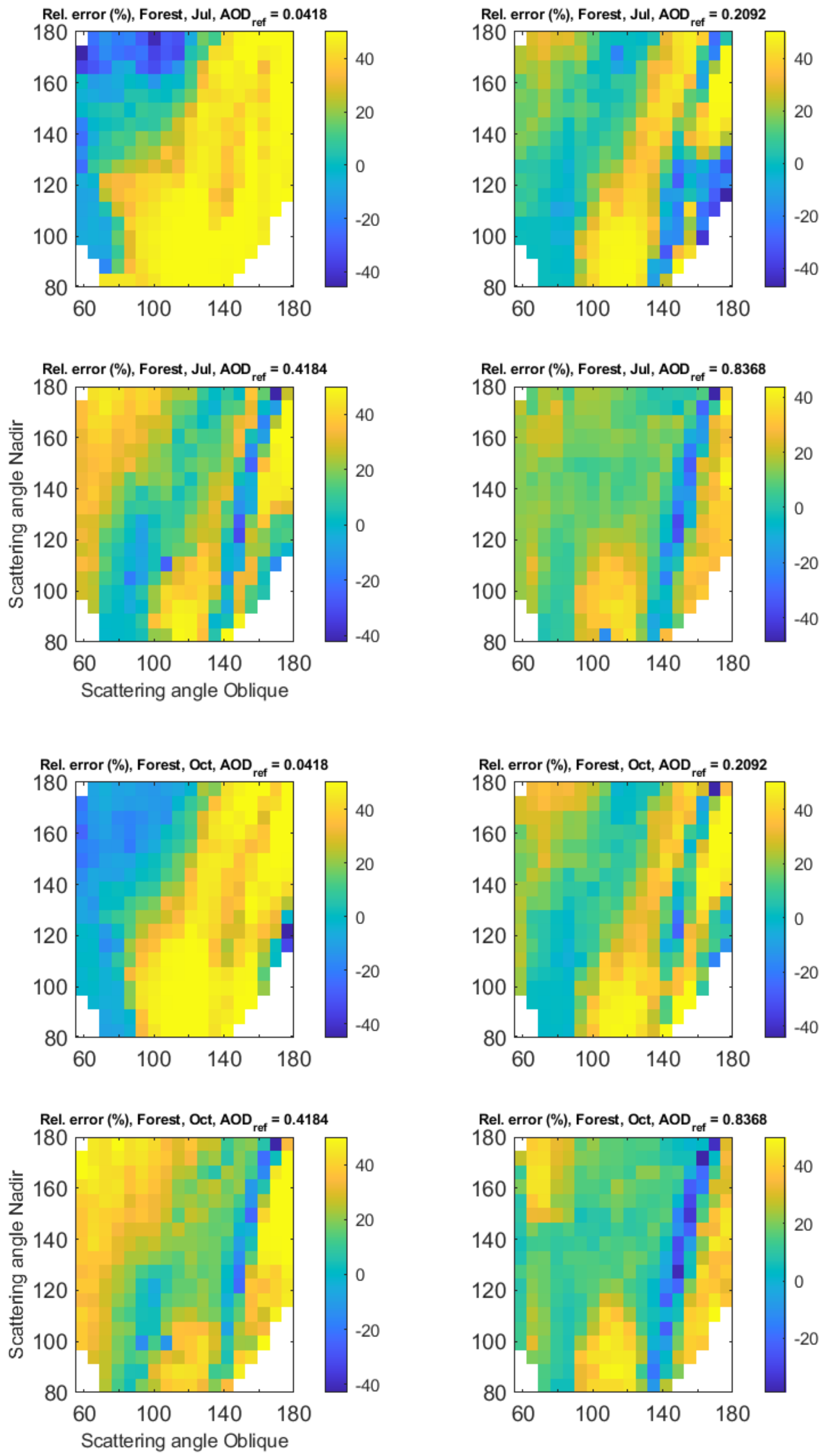
Rel. error (%), Forest, Jul, AOD$_{ref}$ = 0.0418
Rel. error (%), Forest, Jul, AOD$_{ref}$ = 0.2092
Rel. error (%), Forest, Jul, AOD$_{ref}$ = 0.4184
Rel. error (%), Forest, Jul, AOD$_{ref}$ = 0.8368
Rel. error (%), Forest, Oct, AOD$_{ref}$ = 0.0418
Rel. error (%), Forest, Oct, AOD$_{ref}$ = 0.2092
Rel. error (%), Forest, Oct, AOD$_{ref}$ = 0.4184
Rel. error (%), Forest, Oct, AOD$_{ref}$ = 0.8368
Scattering angle Nadir
Scattering angle Oblique

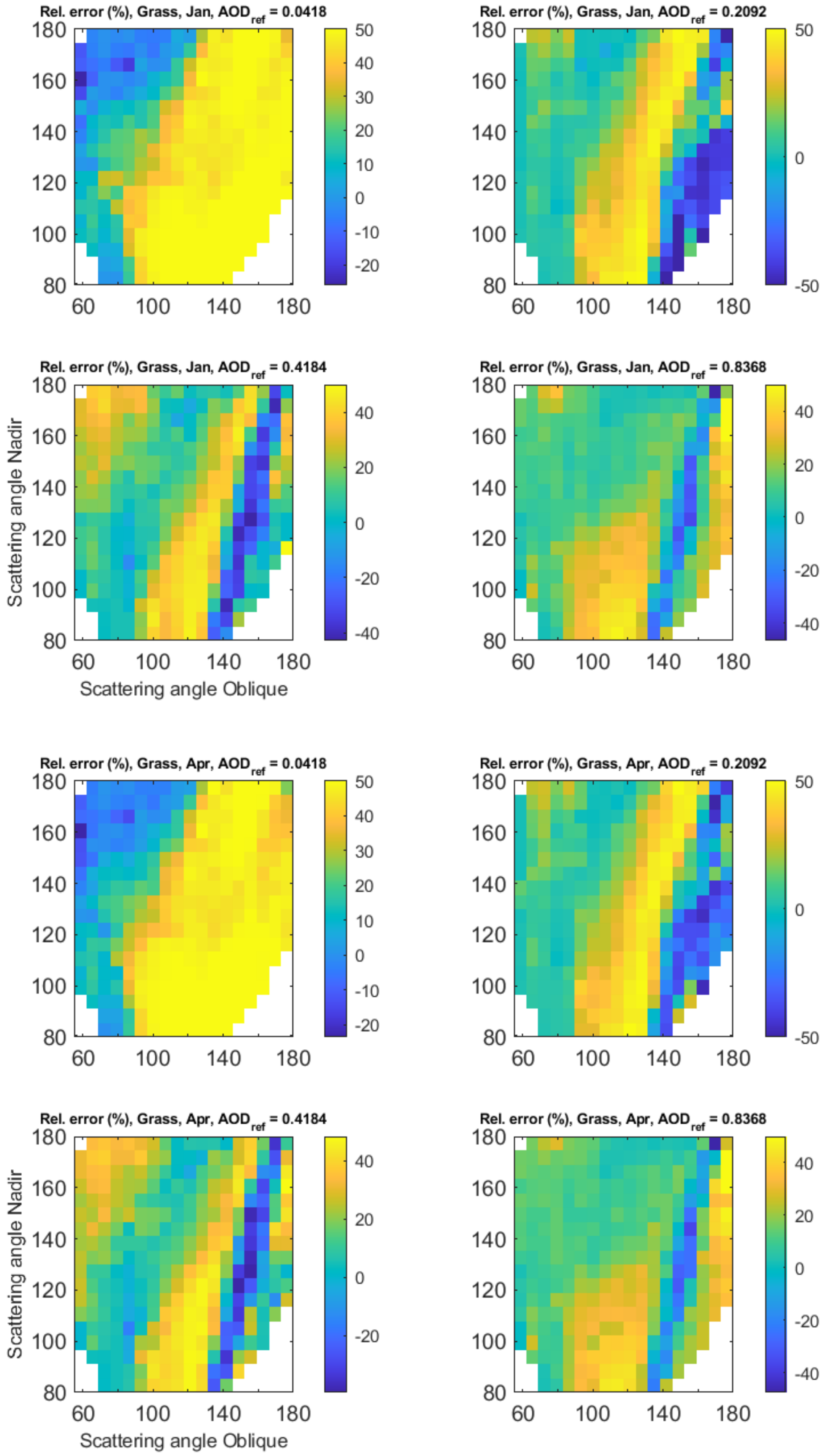
Rel. error (%), Grass, Jan, AOD$_{ref}$ = 0.0418
Rel. error (%), Grass, Jan, AOD$_{ref}$ = 0.2092
Rel. error (%), Grass, Jan, AOD$_{ref}$ = 0.4184
Rel. error (%), Grass, Jan, AOD$_{ref}$ = 0.8368
Rel. error (%), Grass, Apr, AOD$_{ref}$ = 0.0418
Rel. error (%), Grass, Apr, AOD$_{ref}$ = 0.2092
Rel. error (%), Grass, Apr, AOD$_{ref}$ = 0.4184
Rel. error (%), Grass, Apr, AOD$_{ref}$ = 0.8368
Scattering angle Nadir
Scattering angle Oblique

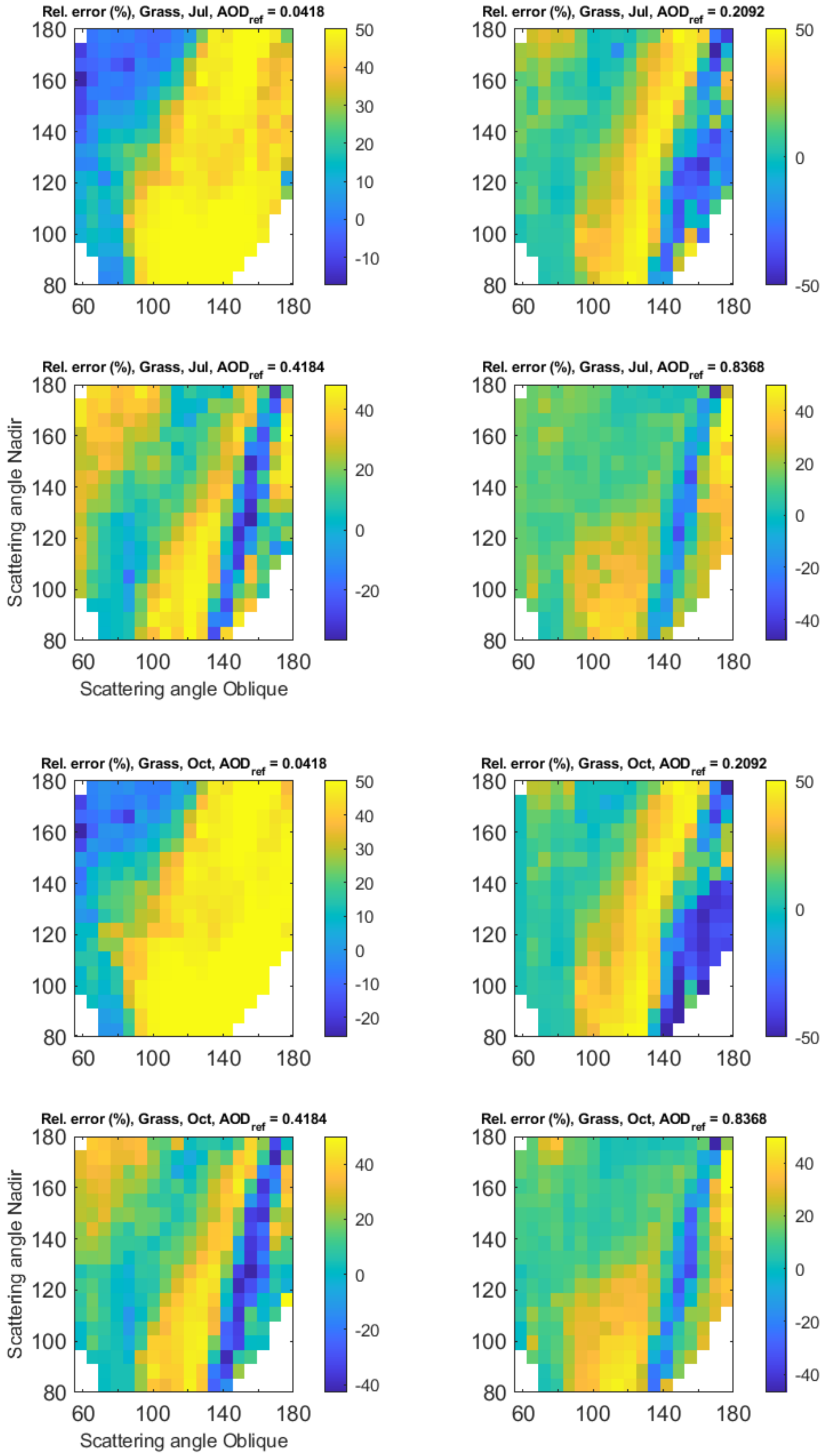

Rel. error (%), Grass, Jul, $AOD_{ref}$ = 0.0418
Rel. error (%), Grass, Jul, $AOD_{ref}$ = 0.2092
Rel. error (%), Grass, Jul, $AOD_{ref}$ = 0.4184
Rel. error (%), Grass, Jul, $AOD_{ref}$ = 0.8368
Rel. error (%), Grass, Oct, $AOD_{ref}$ = 0.0418
Rel. error (%), Grass, Oct, $AOD_{ref}$ = 0.2092
Rel. error (%), Grass, Oct, $AOD_{ref}$ = 0.4184
Rel. error (%), Grass, Oct, $AOD_{ref}$ = 0.8368
Scattering angle Nadir
Scattering angle Oblique

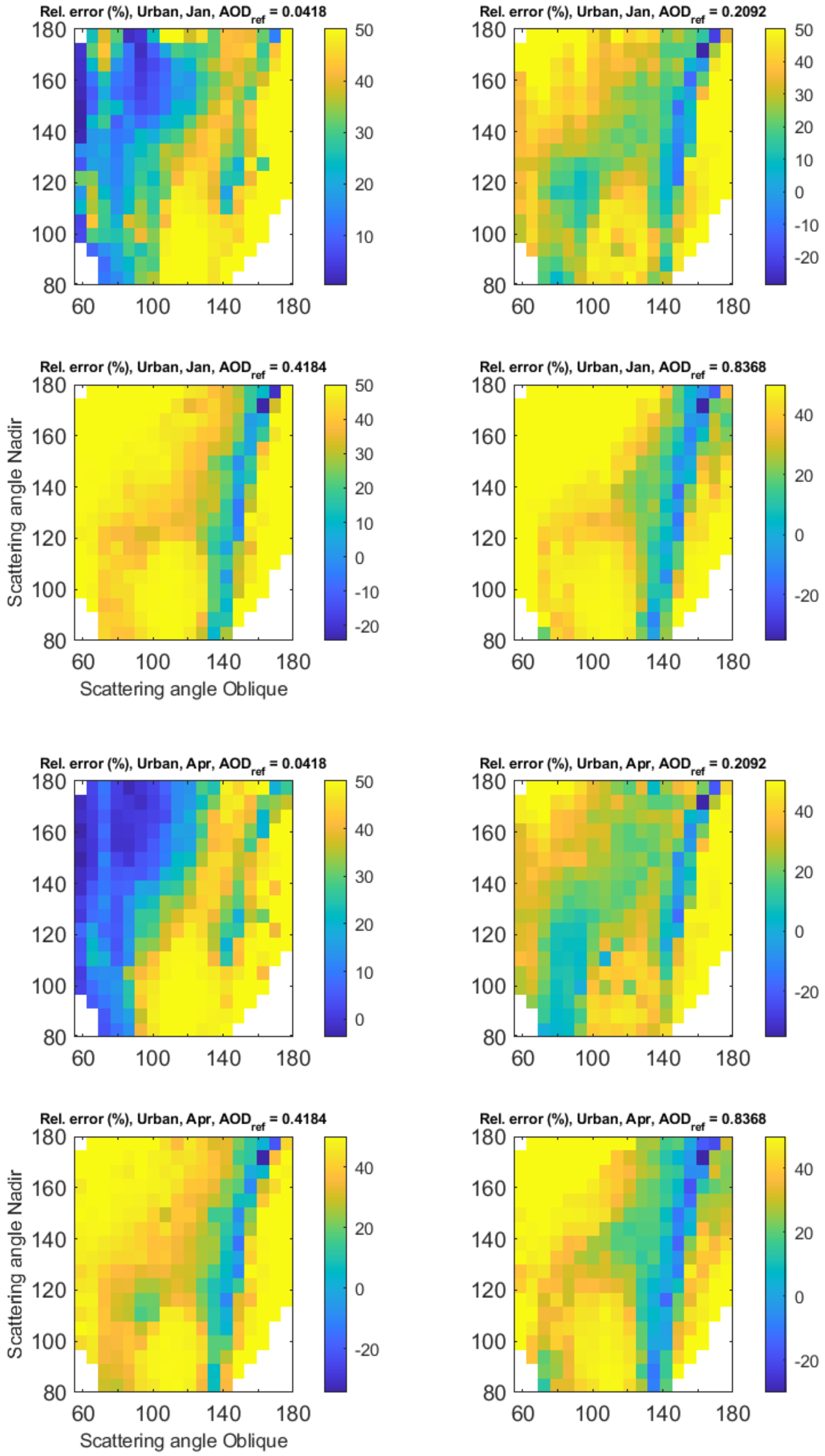
Rel. error (%), Urban, Jan, AOD$_{ref}$ = 0.0418
Rel. error (%), Urban, Jan, AOD$_{ref}$ = 0.2092
Rel. error (%), Urban, Jan, AOD$_{ref}$ = 0.4184
Rel. error (%), Urban, Jan, AOD$_{ref}$ = 0.8368
Rel. error (%), Urban, Apr, AOD$_{ref}$ = 0.0418
Rel. error (%), Urban, Apr, AOD$_{ref}$ = 0.2092
Rel. error (%), Urban, Apr, AOD$_{ref}$ = 0.4184
Rel. error (%), Urban, Apr, AOD$_{ref}$ = 0.8368
Scattering angle Nadir
Scattering angle Oblique

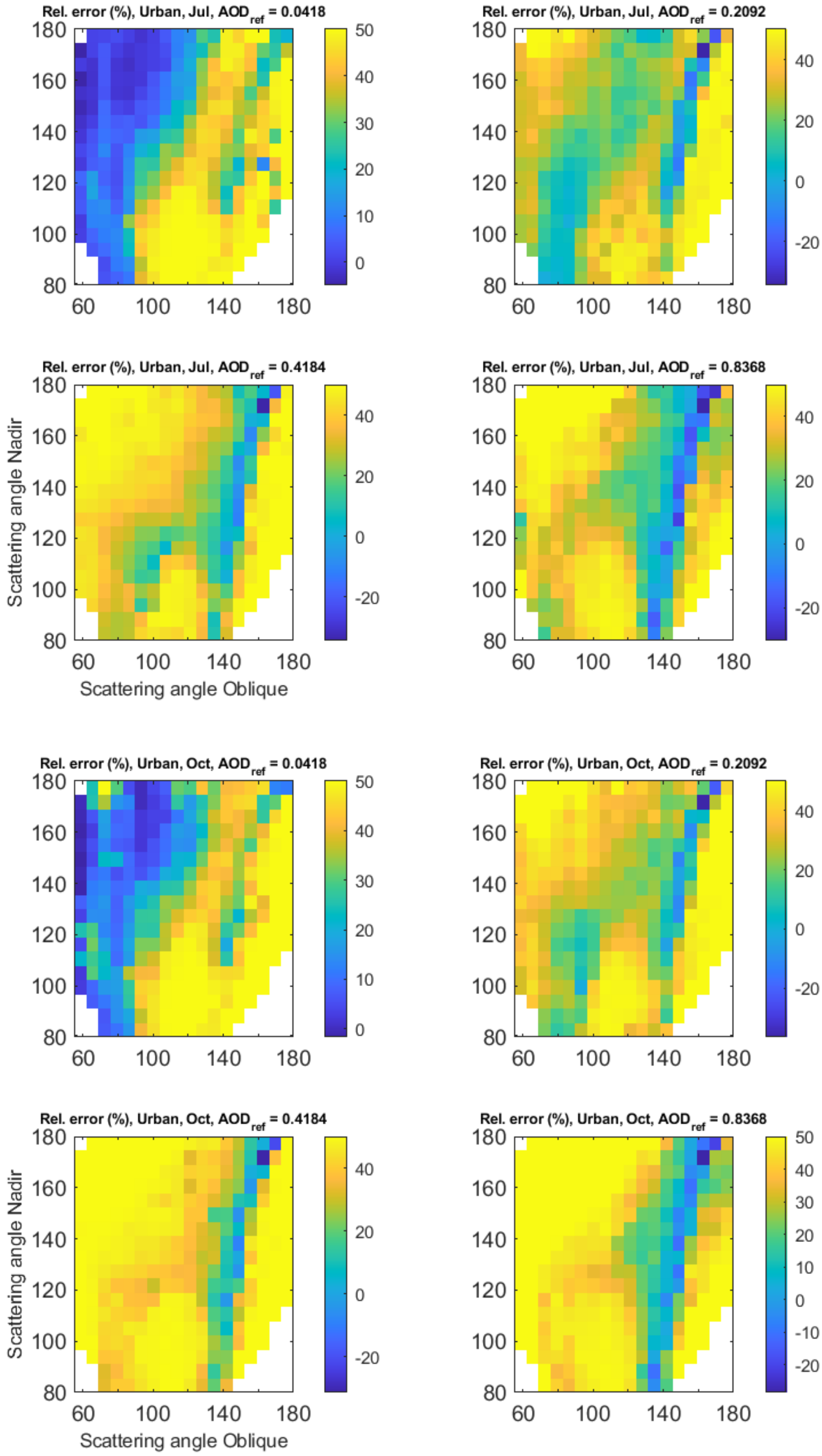
Rel. error (%), Urban, Jul, AOD$_{ref}$ = 0.0418
Rel. error (%), Urban, Jul, AOD$_{ref}$ = 0.2092
Rel. error (%), Urban, Jul, AOD$_{ref}$ = 0.4184
Rel. error (%), Urban, Jul, AOD$_{ref}$ = 0.8368
Rel. error (%), Urban, Oct, AOD$_{ref}$ = 0.0418
Rel. error (%), Urban, Oct, AOD$_{ref}$ = 0.2092
Rel. error (%), Urban, Oct, AOD$_{ref}$ = 0.4184
Rel. error (%), Urban, Oct, AOD$_{ref}$ = 0.8368
Scattering angle Nadir
Scattering angle Oblique

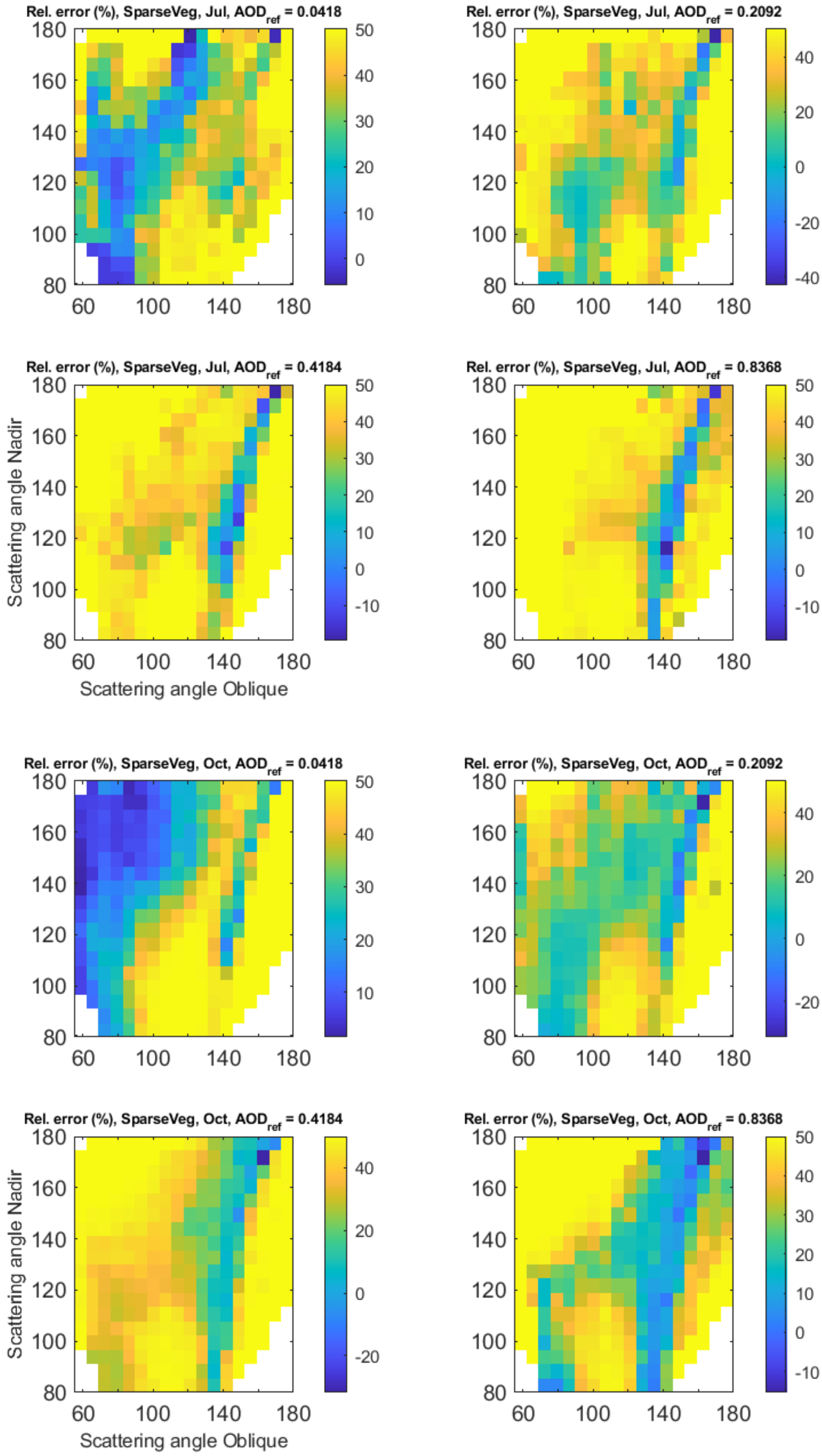
Rel. error (%), SparseVeg, Jul, AOD$_{ref}$ = 0.0418
Rel. error (%), SparseVeg, Jul, AOD$_{ref}$ = 0.2092
Rel. error (%), SparseVeg, Jul, AOD$_{ref}$ = 0.4184
Rel. error (%), SparseVeg, Jul, AOD$_{ref}$ = 0.8368
Rel. error (%), SparseVeg, Oct, AOD$_{ref}$ = 0.0418
Rel. error (%), SparseVeg, Oct, AOD$_{ref}$ = 0.2092
Rel. error (%), SparseVeg, Oct, AOD$_{ref}$ = 0.4184
Rel. error (%), SparseVeg, Oct, AOD$_{ref}$ = 0.8368
Scattering angle Nadir
Scattering angle Oblique

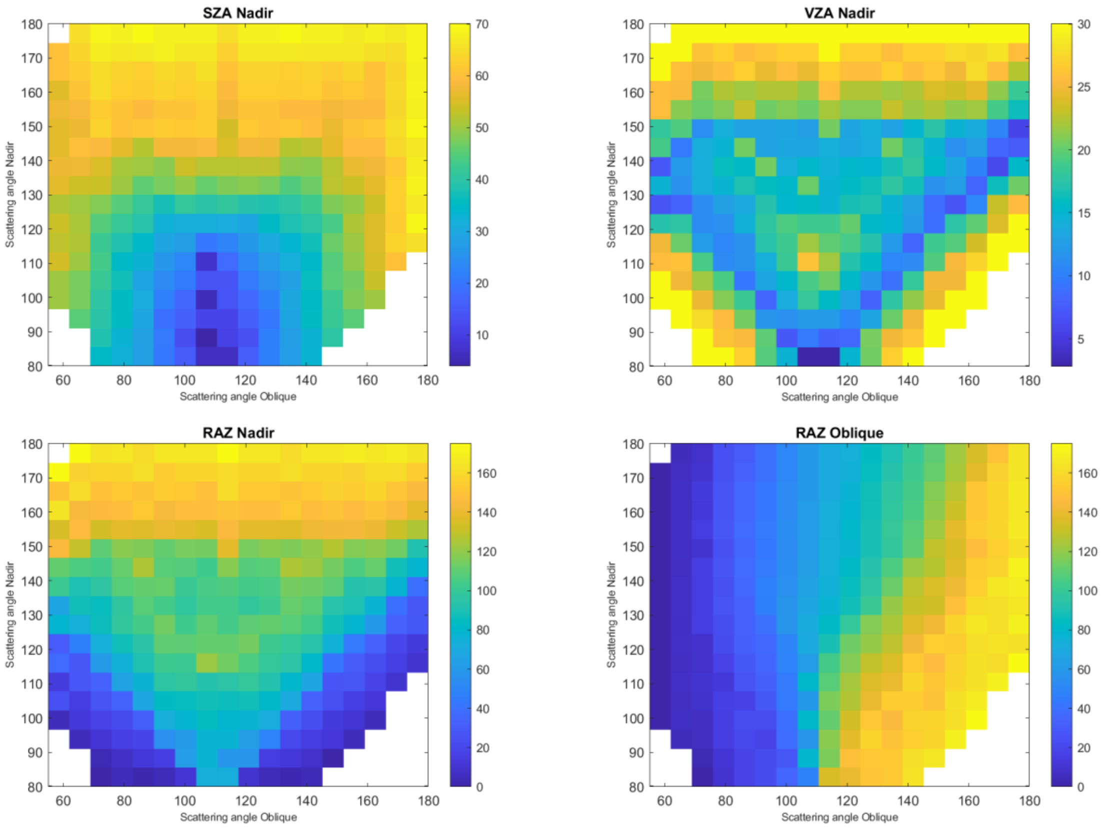


## Appendix: Summary of the AOD retrieval for April 2018 with the new calibration correction

Figure 48 shows the average AOD for April 2018 with the new calibration correction.

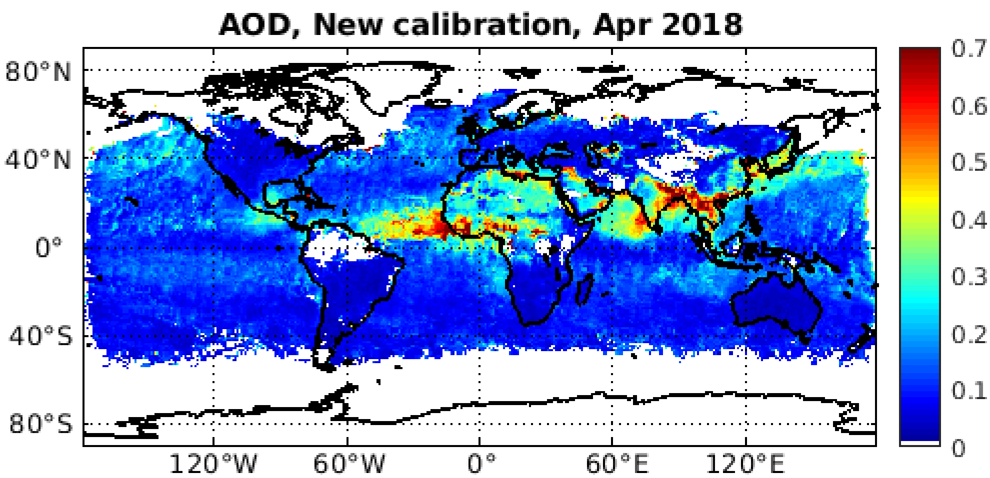


*Figure 48 Average AOD in April 2018 for the new calibration correction.*

Figure 49 shows the AERONET validation and the histogram of the validation error and Figure 50 shows the validation error as a function of the AERONET site latitude. As for the July 2018 validation, small negative bias can be detected.

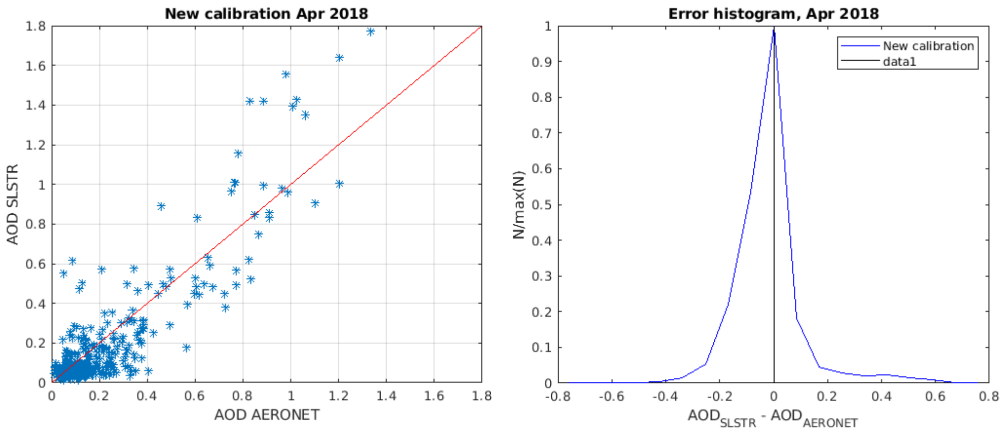


*Figure 49 AERONET validation and error histogram for April 2018.*

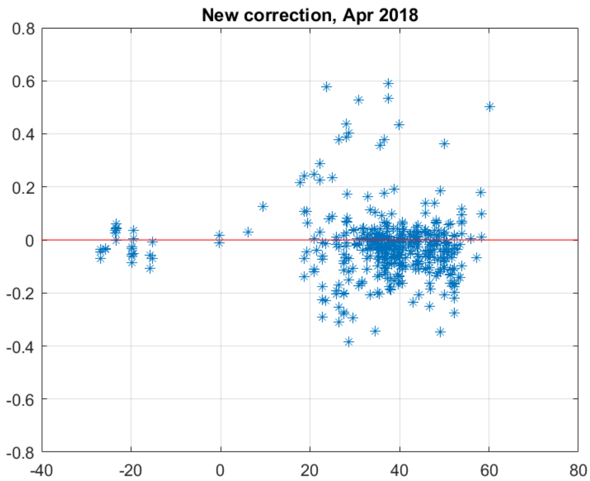


*Figure 50 The validation error for the new calibration correction as a function of the AERONET site latitude.*